



Influence of Molecular Weight between Crosslinks on the Mechanical Properties of Polymers formed via Ring-Opening Metathesis

Journal:	<i>Soft Matter</i>
Manuscript ID	SM-ART-12-2017-002407.R1
Article Type:	Paper
Date Submitted by the Author:	15-Mar-2018
Complete List of Authors:	<p>Long, Tyler; U.S. Army Research Lab, Weapons and Materials Research Directorate Elder, Robert; U.S. Army Research Laboratory Bain, Erich; U.S. Army Research Lab, Weapons and Materials Research Directorate Masser, Kevin; U.S. Army Research Lab, Weapons and Materials Research Directorate Sirk, Timothy; U.S. Army Research Lab, Weapons and Materials Research Directorate Yu, Jian; U.S. Army Research Lab, Weapons and Materials Research Directorate Knorr, Daniel; U.S. Army Research Lab, Weapons and Materials Research Directorate Lenhart, Joseph; USA Army Research Laboratory, ; Sandia National Laboratories,</p>

Influence of Molecular Weight between Crosslinks on the Mechanical Properties of Polymers formed via Ring-Opening Metathesis

Tyler R. Long, Robert M. Elder, Erich D. Bain, Kevin A. Masser, Timothy W. Sirk, Jian H. Yu, Daniel B. Knorr Jr. *, Joseph L. Lenhart*

U.S. Army Research Laboratory,

Aberdeen Proving Ground, MD 21005, USA

*Corresponding authors: Daniel B. Knorr Jr., daniel.b.knorr.civ@mail.mil

Joseph L. Lenhart, joseph.l.lenhart.civ@mail.mil

For submission to Soft Matter

1

Abstract

The apparent molecular weight between crosslinks ($M_{c,a}$) in a polymer network plays a fundamental role in the network mechanical response. We systematically varied $M_{c,a}$ independent of strong noncovalent bonding by using ring-opening metathesis polymerization (ROMP) to co-polymerize dicyclopentadiene (DCPD) with a chain extender that increases $M_{c,a}$ or a di-functional crosslinker that decreases $M_{c,a}$. We compared the ROMP series quasi-static modulus (E), tensile yield stress (σ_y), and fracture toughness (K_{IC} and G_{IC}) in the glassy regime with literature data for more polar thermosets. ROMP resins showed high K_{IC} ($>1.5 \text{ MPa}\cdot\text{m}^{0.5}$), high G_{IC} ($>1000 \text{ J/m}^2$), and 4-5 times higher high rate impact resistance than typical polar thermosets with similar T_g values (100°C to 178°C). The overall E values were lower for ROMP systems. The σ_y dependence on $M_{c,a}$ and $T-T_g$ for ROMP resins was qualitatively similar to more polar thermosets, but the overall σ_y values were lower. In contrast to more polar thermosets, the K_{IC} and G_{IC} values of the ROMP resins showed strong $M_{c,a}$ and $T-T_g$ dependence. High rate impact ($\sim 10^4$ - 10^5 s^{-1}) trends were similar to the K_{IC} and G_{IC} behavior, but were also correlated to σ_y . Overall, a ductile failure mode was observed for quasi-static and high rate results for a linear ROMP polymer ($M_{c,a}=1506 \text{ g/mol}$ due to chain entanglement), and this gradually transitioned to a fully brittle failure mode for highly crosslinked ROMP polymers ($M_{c,a}\leq 270 \text{ g/mol}$). Molecular dynamics (MD) simulations showed that low $M_{c,a}$ ROMP resins were more likely to form molecular scale nanovoids. The higher chain stiffness in low $M_{c,a}$ ROMP resins inhibited stress relaxation in the vicinity of these nanovoids, which correlated with brittle mechanical responses. Overall, these differences in mechanical properties were attributed to the weak non-covalent interactions in ROMP resins.

2

1. Introduction

Crosslinked thermosetting materials are used for a wide range of applications including structural adhesives, fiber reinforced composites, and coatings. Many of these applications require materials that have a combination of high modulus, high strength, high toughness and good impact performance. Unfortunately, high modulus and high strength properties characteristic of highly crosslinked materials are often accompanied by brittle behavior and poor fracture toughness.

The primary method of achieving a balance of these properties is to start with a strong, stiff matrix material and modify this material by adding fillers or co-monomers that toughen the system or impart ductility. These methods include: inducing crystallinity in the system¹, the copolymerization of thermosets with high molecular weight constituents^{2, 3}, as well as the addition of inorganic particles^{4, 5}, core-shell rubber particles^{6, 7}, and elastomers⁸. These techniques have been effective for resins with relatively high M_c and low T_g , but may compromise the desired stiffness or glass transition temperature of the resulting thermosets.

An alternative method is to begin with a resin system that is inherently ductile. Poly(dicyclopentadiene) (pDCPD) is a crosslinked polymer that has emerged as a possible alternative to epoxy resins because pDCPD has demonstrated high toughness and remarkable impact performance yet has a glass transition ($\sim 140^\circ\text{C}$) comparable to brittle structural epoxies.^{9, 10} A unique aspect of pDCPD is that it has no heteroatoms, and therefore lacks strong non-covalent interactions. These types of interactions (e.g., hydrogen bonding) can act as reversible crosslinks¹¹ that influence the polymer dynamic behavior¹², increase the T_g of linear

3

polymers,¹³ and they have been used to form reversible self-assembling polymer systems.¹⁴⁻¹⁷

Within the context of thermosets, molecular dynamics (MD) simulations of pDCPD were compared to those of epoxy systems with comparable crosslink densities, and the results showed significant differences between pDCPD and epoxies in terms of nanovoid volume formation to accommodate strain, indicative of the influence of non-covalent interactions.^{9, 18}

The void formation in pDCPD was energetically neutral, while void formation in the epoxies with similar crosslink densities was energetically unfavorable due to the strong non-covalent interactions in the epoxy that resist void formation.⁹ The combination of a relatively high molecular weight between crosslinks (M_c) and a lack of strong electrostatic interactions in pDCPD suggests that less work is required for the formation of nanovoids. Similarly, the weak non-covalent interactions and higher M_c for pDCPD may facilitate local plastic deformation near the nanovoids, leading to ductile failure. However, there has been no fundamental experimental studies of ductile-to-brittle transitions in ROMP materials or studies focusing on the effect that the molecular weight between crosslinks (M_c) has on the mechanical properties of these non-polar materials.

Such work has been performed for polar systems capable of significant interchain non-covalent interactions such as epoxy networks, wherein hydroxyl groups participate in hydrogen bonding. In a classic work, Crawford and Lesser demonstrated that, for a system of similar epoxy resins, the T_g and yield strength decreased with increasing M_c , while the fracture behavior showed a brittle-to-ductile transition as M_c increased.¹⁹ Elastic properties like the Young's modulus were independent of M_c in epoxy networks, while inelastic properties, like compressive and tensile yield strength, showed an inverse dependence on M_c .²⁰

4

Others have also studied the influence of M_c on the quasi-static fracture toughness, K_{IC} and other mechanical properties. Increases in K_{IC} with M_c were observed for epoxy resins cured with anhydrides in the range of $M_c = 400$ to 1400 g/mol, but little change was observed for the same resin cured with amines for $M_c = 388$ - 539 g/mol.²¹ Fernandez-Nograro et al. found that K_{IC} in diglycidyl ether of bisphenol A (DGEBA)/Jeffamine systems was maximized for M_c values between about 450 and 550 g/mol.²² Cho et al. found a maximum in fracture toughness at 610 g/mol in diallylterephthalate resins.²³ Bell showed that, for amine cured epoxies, the Izod impact strength showed a maximum in M_c at around 1000 g/mol.²⁴ Interestingly, Li and Strachan showed a remarkable change in yield stress at an M_c of about 600 g/mol in MD simulations of an epoxy during curing, which suggests that M_c is correlated with the mechanical properties of reacting systems as well.²⁵

Overall, these works tend to show a dependence of the inelastic mechanical properties (i.e., yield stress, fracture toughness) on M_c . However, the effect of M_c is difficult to isolate in conventional systems like epoxy resins due to the presence of non-covalent interactions like hydrogen bonding, dipole-dipole, and dipole-induced dipole interactions that have been shown to increase T_g values in conventional polymers¹³ and provide glassy-network like properties to supramolecular polymers assembled by non-covalent interactions.¹⁵⁻¹⁷ Polymers like pDCPD present an excellent opportunity to isolate the effects of M_c from changes in polarity because they lack heteroatoms (i.e., N and O) and are largely free of the strong non-covalent interactions found in epoxy resins.¹⁸

5

Here, we focused on the effect that M_c has on mechanical properties and high rate impact resistance of ROMP-based model polymer systems. ROMP polymers were prepared using Grubbs first generation catalyst.²⁶⁻²⁹ There is no typical M_c value for pDCPD because M_c is dictated by the reaction temperature, and monomer to catalyst ratio. These variables do not provide as much range of M_c as desired, so 5-ethylidene-2-norbornene (ENB) and 1,4,4a,5,8,8a-hexahydro-1,4,5,8-dimethanonaphthalene (HDMN) have been utilized. The M_c in these systems was manipulated by copolymerization of pDCPD with ENB, a chain extender used to increase the M_c , and a crosslinker (HDMN, with two isomers) to decrease the M_c (Figure 1). Various combinations of DCPD, ENB, and HDMN have been used previously to manipulate the crosslink density of pDCPD and pENB in a study of self-healing polymer composites, carbon nanotube polymer composites and other ROMP systems.³⁰⁻³⁵ The curing kinetics and thermo-oxidative aging of these ROMP-based systems have also been studied.³⁶⁻⁴¹

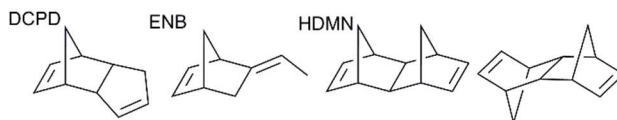


Figure 1. Dicyclopentadiene (DCPD), 5-ethylidene-2-norbornene (ENB), 1,4,4a,5,8,8a-hexahydro-1,4,5,8-dimethanonaphthalene (exo-endo and endo-endo isomers) (HDMN).

In the polymerization of DCPD, the highly strained norbornene ring opens first, followed by opening of the cyclopentene ring to form crosslinks.⁴¹ In the copolymerization of HDMN and DCPD, the opening of the second norbornene ring of HDMN is highly favored over the second ring opening in DCPD, and therefore HDMN is much more likely to create a crosslink site. This is because the rate of ROMP reactions are driven by ring strain.⁴² There is a large difference in ring strain between the second norbornene ring of HDMN and the cyclopentene of pDCPD,

6

where the norbornene has a ring strain of 27.2 kcal/mol, and cyclopentene has a ring strain of only 6.8 kcal/mol.⁴³ In contrast, ENB does not crosslink during ROMP and generates a linear polymer. The polymerization reaction in Figure 2 shows the structures of the copolymers and demonstrates where the crosslinks are formed.

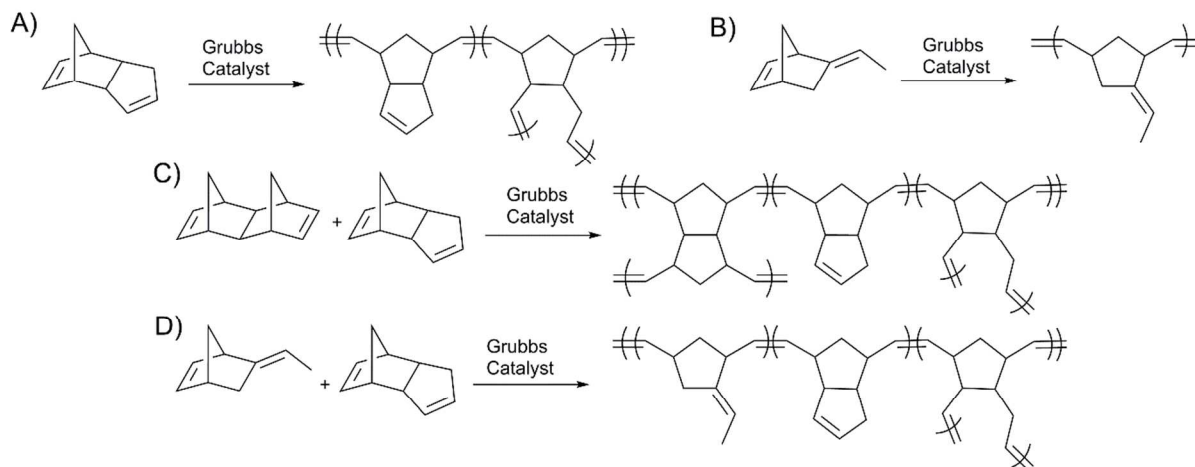


Figure 2. Polymerization of various ROMP-capable monomers illustrating where the crosslinking occurs in A) DCPD, B) ENB, C) HDMN/DCPD mixture, and D) ENB/DCPD mixture.

In this work, a series of ROMP polymers and copolymers were made with a wide range of crosslink densities from highly crosslinked to linear. The performance of these polymers and copolymers was characterized using quasi-static mechanical measurements and high strain rate impact testing. Further, complementary molecular dynamics (MD) simulations were performed to determine the influence of M_c on the molecular behavior of ROMP polymers.

2. Experimental

2.1 Materials and chemical characterization

All chemicals were purchased from Sigma Aldrich and were used as received. The synthesis of HDMN is described in the supplemental information. Dicyclopentadiene contains BHT as a

7

stabilizer and was a solid at room temperature. NMR spectra were acquired using a Bruker 600 MHz UltraShield. The UV-Vis spectra were acquired using a Perkin Elmer Lambda 1050 UV/VIS/NIR spectrometer. The molecular weight of pENB was estimated by size exclusion chromatography – multi-angle light scattering (SEC-MALS) with Wyatt: DAWN HELEOS II, Optilab rEX, and ViscoStar II detectors. These detectors were combined with an Agilent Technologies 1260 Infinity HPLC system that contained an isocratic pump, a thermostatted column compartment, and an auto sampler. Three columns were used, two Polymer Laboratories PLgel 5 μm mixed D columns and one Agilent Technologies MesoPore 3 μm column. The polymer was eluted using THF at a flow rate of 1 mL/min at a column temperature of 30 °C. The molecular weight was determined from the dn/dc value assuming 100% mass recovery.

2.2 Polymerizations

The polymerizations of DCPD, ENB, and copolymers used for high rate impact, thermomechanical characterization, pycnometer, and quasi-static mechanical measurements were made with a total of 2.5 moles of monomers at the mole percent indicated. Polymerizations were conducted for monomer to catalyst ratios of 3000/1, 5000/1 and $10^5/1$. In a typical 5000/1 example, triphenylphosphine (655 mg, 2.5 mmol) was dissolved in the monomer mixture and the mixture was heated to 50 °C. Grubb's 1st generation catalyst (411 mg, 0.5 mmol) was weighed out in an inert gas glove box, then removed from the glove box and dissolved in 8.2 mL of 1,2-dichloroethane to make a 50 mg/mL solution. The catalyst solution was added to the monomer solution and it was gently stirred for about 30 seconds. Then, the solution was poured into a steel mold (15 cm x 15 cm x 0.6 cm). The polymers were cured in a

8

Yamato ADP 21 vacuum drying oven under flowing N₂ for 2 hours at 50 °C, they were then post cured for 2 h at 175 °C. The 10⁵/1 monomer to catalyst case is similar to the above and is described in the supplemental information.

Synthesized linear pENB can be dissolved in solution and was found to be soluble in CHCl₃, CH₂Cl₂, toluene, and THF. pENB (11 mg) was dissolved in THF (1.80 mL) and analyzed by SEC-MALS. We determined that the number average molecular weight (M_n) was 45 kg/mol with a dn/dc of 0.151 and a dispersity of 2.17.

2.3 Thermomechanical characterization

Dynamic mechanical analysis (DMA) was performed on a TA instruments Q800 in 17 mm single cantilever mode to measure storage modulus, loss modulus, and $\tan \delta$. Thick samples (typically 35 mm x 12 mm x 3 mm) were used to measure the rubbery modulus ($T > T_g$), while thin samples (typically 35 mm x 12 mm x 1 mm) were used to measure the glassy modulus ($T < T_g$), in order to obtain a drive force within the optimal compliance range of the instrument for each region. The measurements were taken with a constant displacement of 7.5 μm at a rate of 1 Hz. The storage and loss modulus were measured during a temperature ramp from -100 °C to 250 °C at 1 °C per minute. The glass transition temperature (T_g) was obtained from the peak in the $\tan \delta$ of the thick sample. The room temperature densities of the polymers were measured using a micrometrics Accupyc 1330 pycnometer. Thermomechanical analysis (TMA) was performed on a TA instruments Q400, and the results were used to determine the coefficient of thermal expansion (COTE) to adjust the density for M_c calculations (assuming that the material was isotropic). A heat-cool-heat procedure was used first heating to the post cure temperature to

9

remove thermal history, followed by cooling to -60 °C and finally heating to 250 °C at 3 °C per minute. The values reported are the result of three TMA or DMA runs for each composition.

2.4 Quasi-static mechanical measurements

The quasi-static mechanical measurements were performed on an Instron 5500R model 1125 equipped with a 1000 pound load cell and an oven. Tensile data were obtained using a Type IV specimen dimension according to ASTM D638-10, with a square cross section of 6 mm x 6 mm in the gauge region. The tensile test was performed with a cross head speed of 5 mm/min using DIC (digital image correlation) to obtain the strain values in the elongation and transverse directions. The fracture toughness was measured according to ASTM D5045-99 with a single-edge-notch bending specimen geometry that measured 6 mm x 12 mm x 53 mm. The fracture toughness test was performed with a cross head speed of 10 mm/min and a testing span of 48 mm. The pre-crack was created by inserting a razor blade into the sample (both cooled with liquid N₂) and tapping the razor blade with a hammer to ensure that a natural pre-crack propagated ahead of the razor tip. A minimum of 10 samples were tested for each temperature and composition for both the fracture toughness and tensile measurements.

2.5 High Rate Impact Measurements

High rate impact performance was quantified using the V₅₀BL(P) (ballistic limit, protection criteria, herein abbreviated V₅₀),⁴⁴ which is the velocity at which there is a 50 percent probability of penetrating an aluminum foil witness target behind a sample. This V₅₀ has been used to measure high rate impact response in metals⁴⁵, composites⁴⁶, and polymers⁴⁷. V₅₀ testing is conducted at effective strain rates of 10⁴ – 10⁵ s⁻¹. A more convenient form of the

10

result is the KE_{50} , where $KE_{50}=0.5mV_{50}^2$, and m is the projectile mass. The normalized KE_{50} measurements were obtained by measuring V_{50} using a 0.22 caliber gas gun with a type 302 steel ball bearing as the projectile that measured 5.56 mm in diameter and weighed 0.69 g. The velocity of the projectile was measured by a Doppler radar (BR-3502, Infinition Inc.). The polymer targets (6 cm x 6 cm x 0.6 cm) were fixed between two metal plates with a 5.08 cm diameter circular opening. The impact occurred at an angle perpendicular to the surface. An aluminum foil (0.05 mm thick 2024-T3) witness was placed 5 cm behind the target and was examined after each shot. The V_{50} was calculated by averaging the three lowest velocities where the witness was penetrated by the projectile or a polymer fragment and the three highest velocities where the witness remained intact. The KE_{50} was normalized to the room temperature KE_{50} value of DGEBA/PACM resin discussed in previous work.^{2, 9, 47} A minimum of 12 samples were tested for each temperature and composition.

2.6 Scanning electron microscopy (SEM)

Cross-sections of selected V_{50} samples were prepared by cutting the target in half with a circular saw and sputtering the exposed surface of the penetration cavity with a thin layer of gold-palladium before imaging in a Hitachi S-4700 SEM at 5kV accelerating voltage.

2.7 Molecular dynamics simulations

We conducted atomistic MD simulations of several of the polymers studied in this work. The experimental range of crosslink density was covered by constructing three pDCPD networks with different M_c values by using linear segments composed of n monomers between crosslinkers: pDCPD-1 ($n = 1$, $M_c = 198$ g/mol), pDCPD-3 ($n = 3$, $M_c = 463$ g/mol), and pDCPD-6

11

($n = 6$, $M_c = 859$ g/mol). We constructed 5 replica systems for each M_c to improve statistics. These network structures are identical to those described in our previous work.¹⁰

We also constructed models of linear pENB and linear pDCPD, which represent pDCPD in the limit of low crosslink density. A linear pENB chain of 25 repeat units ($MW \approx 3000$ g/mol) was built with a ratio of $\sim 30:70$ *cis:trans* double bonds randomly dispersed along the polymer backbone. A linear pDCPD chain of 24 repeat units ($MW \approx 3170$ g/mol) was built with all *cis* bonds for consistency with the pDCPD networks.¹⁰ A number N_c of these chains (pENB, $N_c = 392$; pDCPD, $N_c = 376$) were combined to create large systems of $\sim 200,000$ atoms, which were then equilibrated and annealed across the glass transition with the procedure described in our previous work.¹⁰ After annealing, uniaxial extension simulations were conducted at an engineering strain rate of 10^8 s⁻¹ up to 35% strain, following the method in our previous work.¹⁸ This strain rate is necessarily higher than in the experiments because of the limited time scales available in the simulations. We quantified nanoscale voids during deformation as in our previous work.¹⁸

Finally, we constructed smaller polymer models ($\sim 20,000$ atoms) containing a large predefined void using similar methods. The voids were created by a purely repulsive spherical probe with radius 10 Å, which was present through the entire cross-linking and equilibration procedure.

3. Results and Discussion

The M_c values for the polymers discussed in this article were estimated using the theory of rubbery elasticity, Equation 1.^{9, 33, 48} This theory relates the molecular weight between crosslinks or entanglements to the inverse of the modulus in the rubbery region of the DMA

12

measurement. While this theory is not strictly correct for highly crosslinked systems, it can provide an apparent molecular weight between crosslinks or entanglements ($M_{c,a}$) that is useful for qualitative comparisons between these copolymers. In Equation 1, E'_r is the minimum of the storage modulus in the rubbery plateau, T is the absolute temperature where the minimum of the storage modulus is reached, ρ is the density at temperature T , and R is the gas constant ($8.314 \text{ J K}^{-1} \text{ mol}^{-1}$). The density at temperature T of the minimum modulus was calculated from the room temperature density measurement and a correction using the linear coefficient of thermal expansion (COTE) from TMA, assuming the material expansion was isotropic. The glassy COTE of around $90 \text{ }\mu\text{m}/(\text{m }^\circ\text{C})$ was used to adjust the room temperature density to the density at T_g , and the rubbery COTE, which ranged from $150 \text{ }\mu\text{m}/(\text{m }^\circ\text{C})$ to $250 \text{ }\mu\text{m}/(\text{m }^\circ\text{C})$, was used to adjust the density at T_g to the density at the temperature that corresponds to the minimum of the storage modulus. The error in the $M_{c,a}$ measurement is discussed in the supplemental information (Table S1).

$$M_{C,a} = \frac{3\rho RT}{E'_r} \quad 1$$

3.1 Control of $M_{c,a}$ in pDCPD

We initially tried to control $M_{c,a}$ by curing the systems at various temperatures, but this did not provide sufficient control and resulted in sample discoloration (see the discussion of Figure S1 in the supplemental information). Therefore, HDMN was synthesized to provide highly crosslinked formulations to reduce $M_{c,a}$, while ENB was used to produce formulations with

13

higher $M_{c,a}$ values. A more complete discussion of the issues associated with controlling $M_{c,a}$ is provided in the supplemental information.

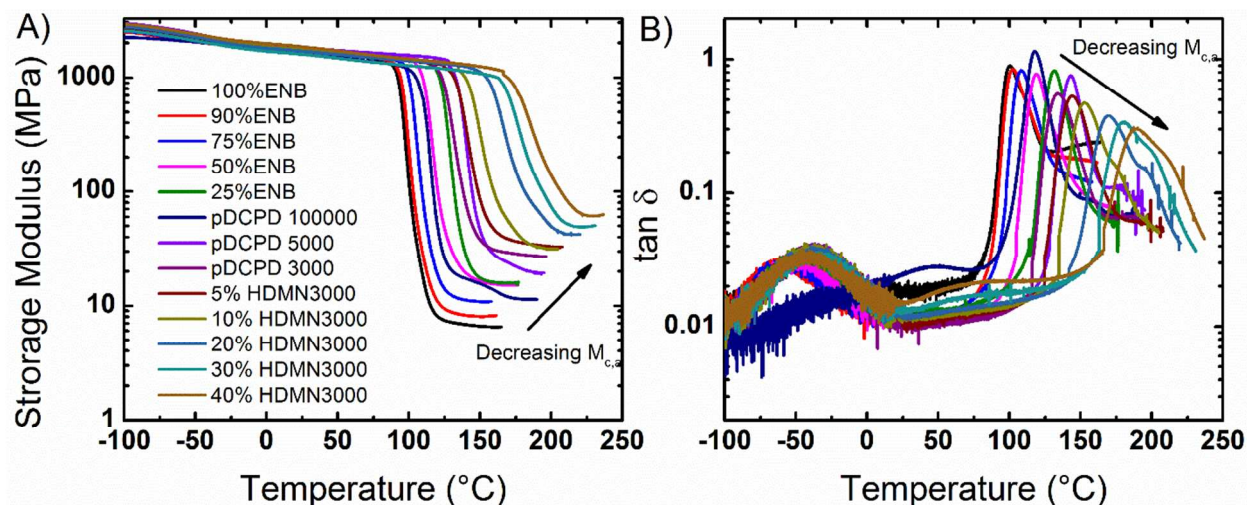


Figure 3. DMA data for a series of the pDCPD copolymers as a function of the concentration of either HDMN or ENB: A) change in storage modulus, B) change in $\tan \delta$.

The DMA data of all the formulations are shown in Figure 3. As shown, the minimum in the storage modulus can be altered by adding ENB or HDMN in pDCPD. DMA data in regions well above the curing temperature may include artifacts related to additional curing, and these data were therefore excluded from Figure 3. The peak in the $\tan \delta$ is also affected by changes in the concentration of the ENB and HDMN in DCPD. ENB/DCPD copolymers were fabricated using a 5000/1 monomer to catalyst loading, and these formulations were post cured at 175 °C. The copolymerization of ENB and DCPD had only a small effect on the $M_{c,a}$ at concentrations where the content of ENB was less than 50 mol%. Lower ENB concentrations did not influence $M_{c,a}$ because of the low initial crosslink density of pDCPD. Therefore, the ENB monomer had to replace a significant amount of the uncrosslinked DCPD monomer before a change in $M_{c,a}$ was observed. A large increase in the $M_{c,a}$ was observed at higher ENB concentrations. pENB (i.e.,

14

100 % ENB) is a linear polymer, where the apparent $M_{c,a}$ is related to the molecular weight between entanglements.

Overall, the copolymerization of DCPD with ENB and HDMN allowed for the fabrication of a series of polymer resins that have similar nonpolar chemical structures and show a range of $M_{c,a}$ values from 204 g/mol to 1506 g/mol (Table 1). The T_g of the DCPD/ENB blends is well-described by the Fox-Flory equation (see Figure S2 in the supplemental information), which suggests that the final polymer is homogeneous (i.e., no phase separation is present).

Table 1. DMA, pycnometer, and TMA results used to calculate $M_{c,a}$ along with the measured normalized KE_{50} . ^aRatio of monomer to catalyst. ^bTested at T_g-75 °C. ^cTested at room temperature. The standard deviation values for the parameters listed here are given in the Supplemental Information (Table S1).

Percent copolymer in pDCPD	M/C^a	T_g (°C)	E' at 25°C (MPa)	E' at T_g-75 °C (MPa)	E' min (MPa)	Density at RT (g/cm ³)	Density at E' min (g/cm ³)	$M_{c,a}$ (g/mol)	^c Normalized KE_{50}
100% ENB	5000	100	1715	1713	6.5	0.972	0.906	1506	3.98±0.10
90%ENB	5000	102	1687	1679	8.1	0.987	0.939	1234	3.98±0.07
75%ENB	5000	108	1713	1681	10.9	1.001	0.944	925	3.98±0.15
50%ENB	5000	119	1795	1725	15.1	1.018	0.950	696	3.69±0.05
25%ENB	5000	132	1721	1593	15.8	1.036	0.978	685	3.58±0.07
pDCPD	10 ⁵	118	1641	1536	11.4	1.041	0.970	976	3.76±0.02
pDCPD	5000	145	1702	1573	18.6	1.044	0.984	597	3.56±0.11
pDCPD	3000	134	1679	1552	27.2	1.062	0.994	428	3.18±0.13
5% HDMN	3000	144	1695	1507	33.1	1.058	0.986	355	3.09±0.19
10% HDMN	3000	153	1744	1519	31.6	1.055	0.994	373	3.18±0.09
20% HDMN	3000	170	1698	1416	42.0	1.055	0.990	288	2.97±0.08
30% HDMN	3000	181	1593	1252	49.0	1.051	0.987	249	2.76±0.08
40% HDMN	3000	187	1853	1408	61.1	1.059	0.994	204	2.25±0.04
10%HDMN ^b	3000	151	1630	1440	27.0	1.061	0.998	432	3.03±0.08

15

20%HDMN ^b	3000	168	1794	1499	39.6	1.061	0.992	304	2.61±0.12
30%HDMN ^b	3000	176	1758	1403	45.2	1.065	0.999	271	2.29±0.09
40%HDMN ^b	3000	178	1946	1507	49.3	1.067	0.998	249	2.14±0.09

The variation in the $M_{c,a}$ for ENB/DCPD and HDMN/DCPD copolymers correlates to a large shift in the T_g as the polymer transitions from a linear polymer to a highly crosslinked network. Figure 4 shows the relationship between $M_{c,a}$ and T_g , with an increase in T_g with increased crosslinking, which is in agreement with previous work on epoxy resins⁴⁹. The lowest T_g was that of pENB (100 °C), which is still high enough to be suitable for many structural applications.

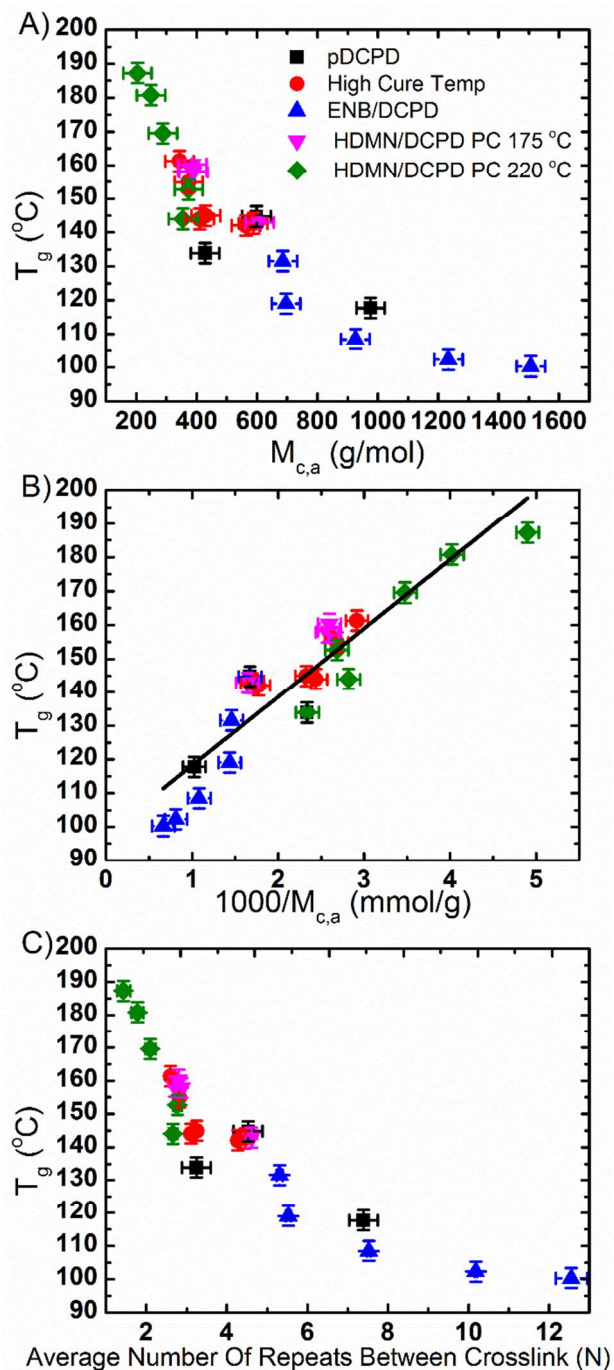


Figure 4. The relationship between A) T_g and $M_{c,a}$, B) T_g and $1/M_{c,a}$, and C) T_g and the average number of repeat units between crosslinks for the pDCPD series (black), the ENB/DCPD copolymers (red), the HDMN/DCPD copolymers post-cured at 175°C and a 5000/1 catalyst loading (blue), and the HDMN/DCPD copolymers post-cured at 220°C and a 3000/1 catalyst loading (green).

In addition to the mixtures of DCPD with ENB and mixtures of DCPD with HDMN, the molecular weight between crosslinks was varied for neat DCPD by controlling the polymerization

17

conditions. pDCPD formulations with $M_{c,a}$ values ranging from 428 g/mol to 976 g/mol were generated as a control. These results are shown in Figure 4 (black data), where the T_g of this series of pure DCPD polymers followed the trends of the remainder of the materials investigated here. The neat DCPD results suggest the trends observed in both the T_g and the KE_{50} are not an artifact of differences in network structure or chain rigidity caused by the comonomers.

The molecular weight dependence of T_g was treated in a manner similar to Fox and Flory, who investigated the dependence of T_g on the molecular weight of unentangled polymers.^{50, 51}

$$T_g = T_{g,\infty} - \frac{K}{M_c} \quad 2$$

Where $T_{g,\infty}$ is the T_g at infinite molecular weight between crosslinks, and K is a material parameter. A fit to the data in Figure 4B yields a K parameter of $-21,000 \pm 2,000$ and a $T_{g,\infty}$ of $92 \text{ }^\circ\text{C} \pm 5 \text{ }^\circ\text{C}$. This treatment differs from that of Fox and Flory in that they investigated thermoplastic melts relative to the entanglement molecular weight, M_e , whereas these materials are thermosets, and the T_g measured here involves motion of a network structure, not simply individual, fixed chains. For thermoplastics below M_e , the T_g was observed to be linearly proportional to $-1/M$ (molecular weight), but the network T_g exhibits the opposite trend (i.e., it is proportional to $+1/M_{c,a}$) as shown in Figure 4B. The reversal in the dependence of T_g on $M_{c,a}$ is expected, since, unlike the diluent effect of chain ends in a disentangled melt ($M < M_e$), the chain ends in these systems are tethered to each other, and would therefore have a restricting effect on chain motion. As $M_{c,a}$ decreases, the restricted motion of the chain ends would effectively increase T_g , as is commonly observed in thermosets with lower molecular

18

weights between crosslinking junction points.⁵² The theoretical $T_{g,\infty}$ of $92\text{ }^{\circ}\text{C} \pm 5\text{ }^{\circ}\text{C}$ at infinite molecular weight is slightly lower than T_g of neat pENB, which has a T_g of $100\text{ }^{\circ}\text{C} \pm 2\text{ }^{\circ}\text{C}$, but is in reasonable agreement.

Figure 4C shows the T_g as a function of the average number of repeats between crosslinking junction points, N . N is a simple weighted average based on the monomer feed ratios. As shown, the T_g continuously increases with decreasing N , with more rapid increases coming below an N value of about 6. As will be shown in the modeling section below, an N value of 5-6 repeat units is close to the length scale over which orientational correlation is lost in pDCPD.

3.2 Quasi-static mechanical properties

In this section we compare the quasi-static mechanical properties of our synthesized ROMP resins to those of conventional thermosets. Quasi-static tensile properties (modulus and yield stress), critical stress intensity factor (K_{IC}) and critical strain energy release rate (G_{IC}) were measured for the ROMP materials at both room temperature and in an oven at various temperatures T such that $T - T_g = \text{constant} = -75^{\circ}\text{C}$ (corresponding to room temperature for 100% pENB, the formulation with lowest T_g). These data are summarized in Table 2. In Figure 5 these data are compared with common thermosetting materials containing polar components (e.g., epoxies cured with anhydrides and amines and diallylterephthalate resins), where they are plotted as a function of both $M_{c,a}$ and $T - T_g$ to illustrate the effects of chain architecture, chemistry, and temperature on the mechanical response.

As shown in Figure 5A and B, the modulus of the ROMP resins at room temperature does not depend strongly on $M_{c,a}$ or $T - T_g$, which is consistent with previous observations for epoxy

systems²⁰. Overall, the glassy moduli of the ROMP resins are generally lower than that observed for epoxy systems, and this is likely due to their weak non-covalent interactions.

Table 2. Quasi-static mechanical properties.

Polymer	T °C	Young's modulus (MPa)	Yield Stress (MPa)	K _{IC} (MPam ^{1/2})	G _{IC} (kJ/m ²)
pENB ^a	RT=T _g -75 °C	1987±79	49.1±0.5	3.16±0.12	4.55±0.37
90%ENB ^a	RT	1974±36	49.5±0.4	3.18±0.16	4.53±0.37
75%ENB ^a	RT	1972±34	50.6±0.5	2.67±0.13	3.52±0.35
50%ENB ^a	RT	2004±28	52.6±0.2	2.42±0.17 ^d	2.77±0.47 ^d
25%ENB ^a	RT	1931±32	52.7±0.3	2.08±0.23 ^d	2.25±0.37 ^d
pDCPD ^a	RT	1851±113	54.8±0.4	2.08±0.22	2.25±0.38
10%HDMN ^b	RT	1871±37	54.2±0.3	1.38±0.19	1.02±0.23
20%HDMN ^b	RT	1985±58	56.5±1.1	1.11±0.05	0.67±0.06
30%HDMN ^b	RT	2044±41	58.1±2.0	0.94±0.03	0.43±0.04
40%HDMN ^b	RT	2123±70	N/A ^c	0.81±0.04	0.31±0.02
90%ENB	T _g -75°C	2022±38	49.5±0.3	3.19±0.22	4.66±0.72
75%ENB	T _g -75°C	2021±49	49.2±0.8	2.62±0.23 ^d	3.42±0.54 ^d
50%ENB	T _g -75°C	1974±38	47.6±0.3	2.43±0.15 ^d	2.91±0.36 ^d
25%ENB	T _g -75°C	1852±96	45.1±1.1	2.32±0.16 ^d	3.01±0.32 ^d
pDCPD ^a	T _g -75°C	1693±114	43.3±0.6	2.20±0.27 ^d	2.96±0.34 ^d
10%HDMN ^b	T _g -75°C	1669±92	40.6±0.3	1.83±0.11 ^d	2.38±0.26 ^d
20%HDMN ^b	T _g -75°C	1555±181	39.3±0.2	1.64±0.02 ^d	1.88±0.12 ^d
30%HDMN ^b	T _g -75°C	1583±56	36.8±1.1	1.47±0.06	1.48±0.16
40%HDMN ^b	T _g -75°C	1668±58	35.9±1.7	1.34±0.04	1.17±0.09

^a monomer to catalyst ratio 5000/1.

^b monomer to catalyst ratio 3000/1.

^c broke before yielding.

^d not strictly valid according to the ASTM D5045-99 due to tearing during the test.

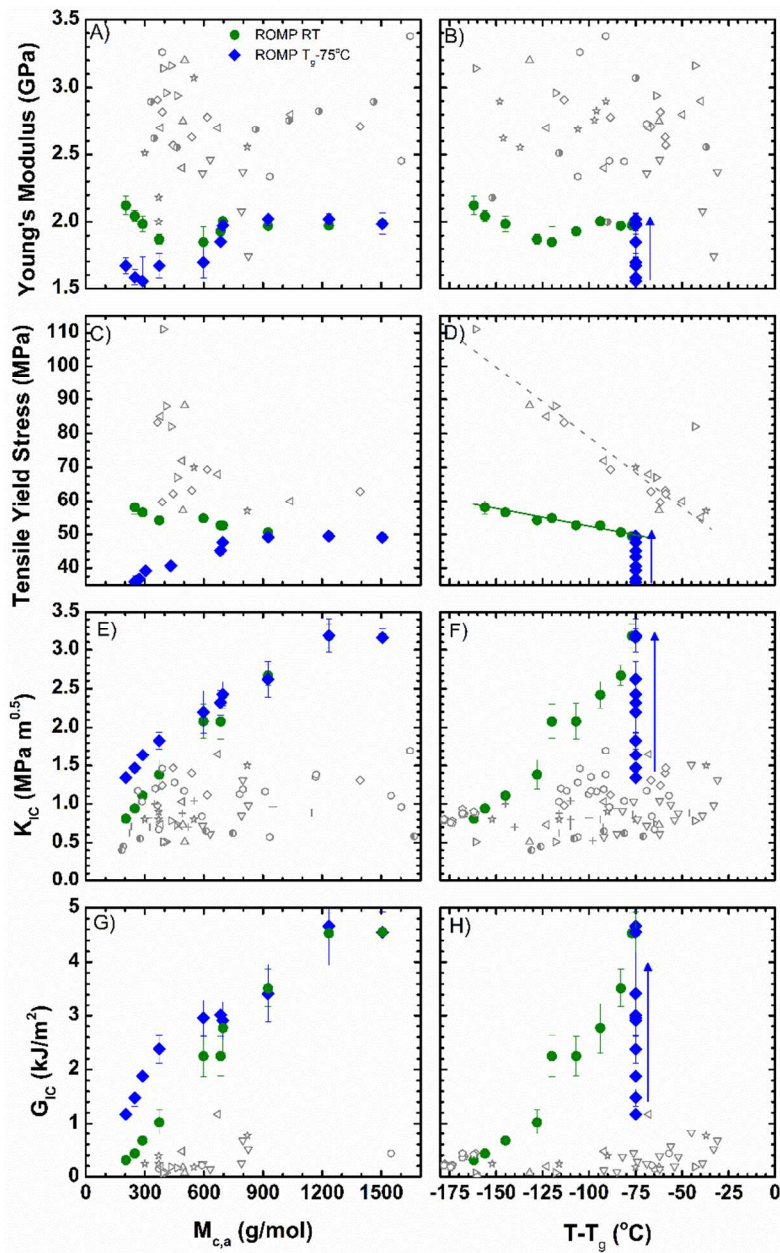


Figure 5. Plots of (A, B) Young's modulus, (C, D) tensile yield stress, (E, F) K_{IC} and (G, H) G_{IC} as a function of $M_{c,a}$ (left column) and measurement temperature minus the material T_g ($T-T_g$, right column). ROMP data are provided at both room temperature (filled green circles) and $T_g-75^\circ\text{C}$ (filled blue diamonds). The lines in (D) are a guide to the eye to illustrate differences in slope between nonpolar ROMP resins and more polar thermosets. The blue arrows in the $T-T_g$ plots show the direction of increasing $M_{c,a}$ for the $T_g-75^\circ\text{C}$ data. The gray data are room temperature data for non-ROMP systems including: amine-cured epoxy resins, anhydride-cured epoxies and diallylterephthalate resins corresponding to the following references: \square^5 , \bullet^6 , \triangleleft^{19} , \diamond^{21} , \circ^{23} , \circ^{24} , $|^{53}$, $-^{54}$, $+^{55}$, \times^{56} , \circ^{57} , Δ^{58} , \triangleright^{59} , ∇^{60} , \ast^{61} , hexagons⁶² and pentagons⁶³. Note that some of the M_c values from the references are theoretical.

Tensile yield stress, σ_y , is shown for the ROMP resins in Figure 5C and D. At room temperature, σ_y of the ROMP resins increases as $M_{c,a}$ decreases, which is consistent with most observations

21

for epoxy networks²⁰. This trend is usually explained¹⁹ in terms of variations in T_g as a function of M_c , based on the assumption that yield stress depends only on $T-T_g$ for networks of similar chemistry^{19, 64, 65}. However, for the ROMP networks a positive and systematic trend was observed between M_c and σ_y when tested at constant $T-T_g = -75^\circ\text{C}$ (blue filled diamonds in Figure 5C), challenging this assumption. Figure 5D shows a linear dependence of room temperature σ_y on $T-T_g$ for both ROMP materials and more polar thermosets from the literature. However as illustrated by the lines in Figure 5D, ROMP resins exhibit a much weaker $T-T_g$ dependence of yield stress than the more polar thermosets. In addition, the variation in σ_y at constant $T-T_g = -75^\circ\text{C}$ (~ 15 MPa) is actually greater than the total variation over the range $-156^\circ\text{C} \leq T-T_g \leq -75^\circ\text{C}$ at room temperature (~ 10 MPa). Taken together, these trends suggest the relationship between yield stress and M_c in ROMP resins is more complex than is commonly assumed for network polymers. While yield stress does correlate weakly with $T-T_g$, shifts in T_g alone are not sufficient to fully explain the trends, since yield stress also varies systematically at constant $T-T_g$ (Figure 5C) with a greater extent of variation than that at varying $T-T_g$ over the same range in $M_{c,a}$. Figure S3A in the supplementary information provides further evidence for this argument, showing that σ_y varies approximately linearly with measurement temperature T at $T = T_g - 75^\circ\text{C}$.

Quasi-static K_{IC} and G_{IC} values for ROMP resins and various polar crosslinked systems reported in the literature are shown as a function of $M_{c,a}$ and $T-T_g$ in Figure 5E through H. Interestingly, the room temperature K_{IC} values for the ROMP resins are similar to that of the more polar networks below a $M_{c,a}$ of about 400 g/mol, suggesting that $M_{c,a}$ may be a primary factor influencing K_{IC} in this region. The ROMP and polar polymer data diverge above an $M_{c,a}$ of

22

approximately ~ 400 ($N \sim 4-5$). Another interesting point is that the K_{IC} and G_{IC} values for the ROMP resins increase with increasing $M_{c,a}$, but the polar thermosets do not show trends that are as strong (Figure 5E and G). Furthermore, the K_{IC} and G_{IC} values of the polar thermosets show weaker $T-T_g$ dependence as compared to the ROMP resins (Figure 5F and H). A common hypothesis in the literature^{60, 61} is that energy dissipation in the crack tip plastic zone depends primarily on the accessibility of plastic deformation processes which are thermally activated and stress state dependent. Hence, fracture toughness values for epoxy networks typically collapse onto a single curve as a function of yield stress.^{19, 64, 65} As shown in Figure S3B in the supplementary information, ROMP polymers generally follow this trend at room temperature, yet at $T_g-75^\circ\text{C}$ they follow an opposite trend, with increasing K_{IC} as a function of σ_y . This observation suggests the need for further research to elucidate the mechanisms of deformation and fracture in highly nonpolar network polymers.

Overall, a comparison of the quasi-static results between ROMP resins and epoxy resins over a comparable $M_{c,a}$ and $T-T_g$ ranges shows that: (i) the ROMP resins generally have a lower modulus, (ii) the ROMP resins generally have a lower yield strength with a weaker yield strength dependence on $M_{c,a}$ and $T-T_g$ at room temperature (which suggests a weaker temperature dependence), (iii) the ROMP resins have similar K_{IC} and G_{IC} values to the more polar materials for $M_{c,a} < \sim 400\text{g/mol}$, and (iv) K_{IC} and G_{IC} values for ROMP resins are much higher than the polar thermosets for $M_{c,a} > \sim 400\text{g/mol}$ and show strong $M_{c,a}$ and $T-T_g$ dependence while the more polar resins do not show this dependence. Collectively, all of these data illustrate that there is a fundamental difference between ROMP resins and their polar counterparts.

Overall, our goal is to maintain matrix ductility and fracture toughness deep in the glassy state while maintaining a high T_g . The two most common ways of increasing matrix ductility and fracture toughness in conventional polar resins (e.g., epoxies) are to (i) increase the M_c and (ii) reduce monomer stiffness (for example by inserting flexible monomers). However, both of these methods result in rather dramatic reductions in T_g . Increasing M_c clearly decreases T_g as shown in previous epoxy literature⁴⁹. As an example of reducing monomer stiffness, curing DGEBA with a rigid aliphatic cyclic diamine (i.e., PACM, molecular weight=210.36 g/mol) results in a T_g of 164°C, while replacing PACM with a flexible polyether diamine of similar molecular weight (i.e., D230, molecular weight= \sim 230 g/mol) yields a T_g of 96°C⁹, indicating a significant reduction in T_g . This trade-off is readily illustrated in Figure 6, where our desirable ductility (low yield stress) and high fracture toughness (i.e., moving from right to left along the dotted gray line) come at a significant T_g penalty for various epoxy systems. For example, the epoxy resins in Figure 6 that exhibit K_{IC} near and above 1 MPa·m^{0.5} generally have T_g values less than 100°C.

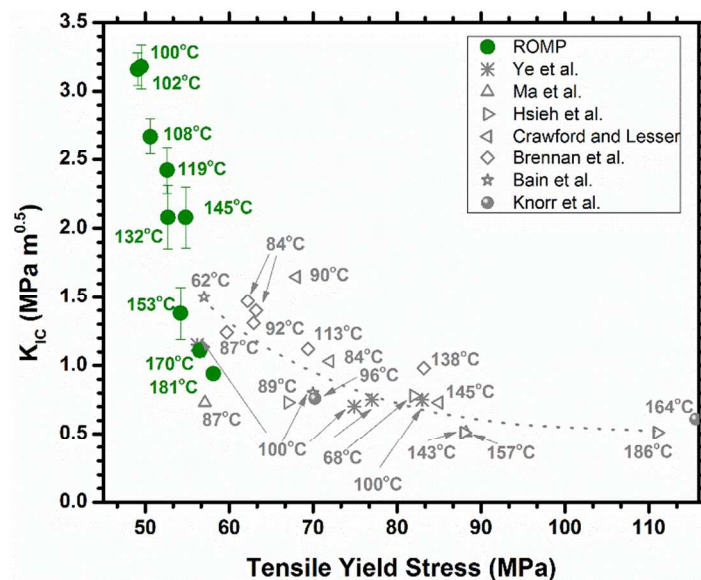


Figure 6. K_{IC} as a function of tensile yield stress for ROMP polymers at room temperature and various epoxy thermosets. T_g values for each point are given as indicated. Symbol designations correspond to the same references in Figure 5 except for the filled gray circles from⁹. Note that the filled gray symbol at 164°C corresponds to a compressive yield stress because this polymer (DGEBA/PACM) did not yield in tension, but failed in a brittle manner.

An alternative option for maintaining high T_g and ductility is to modify the non-covalent interactions within the network, which results in the low yield stress and high K_{IC} values of the ROMP resin shown in Figure 6. As shown, the ROMP resins follow the same general trend for yield stress as a function of toughness implied in the work of Crawford and Lesser¹⁹, but show high T_g values, in some cases 70 °C to 90 °C higher than epoxy resins with similar yield stress and K_{IC} values. To demonstrate that there is a significant difference in polarity between the types of resins shown in Figure 6, we used the cohesive energy density (CED) of a network, which is the increase in internal energy if all intermolecular forces are eliminated⁶⁶. Therefore, the CED provides a relative indication of the strengths of the non-covalent interactions, with lower values indicating weaker non-covalent interactions. We estimated the cohesive energy density (CED) of two non-polar ROMP systems, pDCPD ($M_{c,a}=597$, $T_g=145^\circ\text{C}$) and linear pENB ($T_g=100^\circ\text{C}$) and compared these to two representative epoxy/amine systems that are shown as filled gray

25

circles in Figure 6 and have been studied in our previous work⁹, i.e., DGEBA cured with either PACM or D230 mentioned above. Group contribution methods of Fedors⁶⁷ and van Krevelen⁶⁶ were used to calculate the molar cohesive energy, E_{coh} , while the measured polymer density, ρ , and molar mass of the repeat unit, M_m , were used in the final calculation of cohesive energy density $\text{CED} = \rho E_{\text{coh}} / M_m$ as suggested previously⁶⁸. The CED values from the van Krevelen (Fedors) methods were 249 (336) MPa for pDCPD, 204 (286) MPa for pENB, 383 (477) MPa for DGEBA/D230 and 415 (424) MPa for DGEBA/PACM. These values clearly show that the ROMP resins have significantly lower CED values and therefore are expected to have significantly weaker non-covalent interactions. Therefore we conclude that the reason for the simultaneously high glass transition temperature and high toughness of the ROMP resins is that the weak non-covalent interactions facilitate a lower yield stress. In the framework developed by Lesser and Calzia⁶⁹, which accounts for network behavior using CED to reflect network strength and T_g to reflect network stiffness, the ROMP resins manage to maintain network stiffness (T_g) while reducing network strength (CED).

Other factors that could account for these differences include chain packing, chain architecture, chain stiffness, and crosslink functionality. Indeed, epoxy-amine systems polymerize in a step-growth manner, whereas ROMP systems polymerize in a chain-growth manner, and this may lead to a different polymer architecture or distribution of crosslink junctions. Our MD results below show that the chain stiffnesses of the ROMP resins are comparable to at least some epoxy systems, and our focus on $M_{c,a}$ attempts to account for changes in crosslink functionality. While it is difficult to completely eliminate influences other than non-covalent interactions, it must be noted that a variety of chemistries and functionalities are represented by the polar

26

materials in Figure 5. Given that the common link in these materials is the significantly greater polarity and higher CED than the ROMP resins, and in light of the literature demonstrating the tendency of noncovalent interactions among polar functional groups to act as reversible crosslinks^{11, 12, 14}, the absence of strong noncovalent interactions in ROMP resins is therefore likely to be an important cause for the significant differences observed in their mechanical and fracture properties from those of conventional systems.

3.3 High strain rate impact results

The impact performance of polymers and composites at high strain rate depends on several energy dissipation mechanisms.^{70, 71} Epoxy resins are often utilized because they meet the strength and stiffness requirements for structural applications. The KE_{50} of epoxy resins has shown strong temperature dependence, and segmental relaxations play a key role in the ballistic performance.^{2, 47, 52} However, epoxy resins tend to exhibit brittle fracture during a high rate impact event.

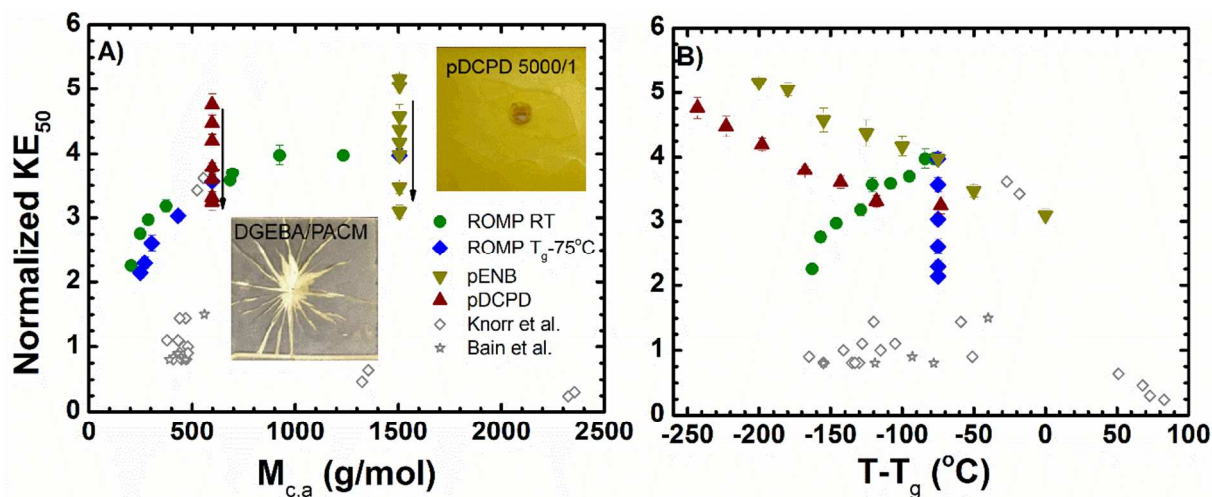


Figure 7. A) Normalized KE_{50} of ROMP resins as a function of $M_{c,a}$ compared with epoxy data from^{6, 47}. The arrows show the direction of increasing measurement temperature for the pENB and pDCPD series. Note that M_c data from⁴⁷ are theoretical. B) Normalized KE_{50} of ROMP resins as a function of $T-T_g$ compared with epoxy data from the literature.

27

Figure 7 provides a comparison of the high rate data obtained for the ROMP systems with those of conventional polar materials in the same format as Figure 5. As shown in Figure 7A, the ROMP resin KE_{50} behavior with respect to $M_{c,a}$ is similar to that of the K_{IC} and G_{IC} behavior in Figure 5E and F. As with K_{IC} and G_{IC} , the epoxy systems generally show much lower values than the ROMP systems with the exception of a few points associated with a formulation near its T_g , where it behaves in a more ductile manner⁴⁷. KE_{50} measurements for pDCPD and pENB were performed over a wide temperature range, and these data are in the form of a vertical KE_{50} series for a single $M_{c,a}$ in Figure 7A. These data illustrate the influence that temperature can have for a single formulation (i.e., a single $M_{c,a}$).

KE_{50} data are shown in Figure 7B as a function of $T-T_g$. Again, the ROMP series data (both RT and $T_g-75^\circ\text{C}$) are reminiscent of the K_{IC} and G_{IC} behavior observed in Figure 5F and G. Interestingly, the data for specific formulations (pENB and pDCPD) are similar to the behavior of the yield stress shown in Figure 5D. The relationship between K_{IC} , yield stress and KE_{50} will be discussed in the next section. Again, these data suggest that the behavior of ROMP resins is fundamentally different from more polar epoxy resins even when the effects of $M_{c,a}$ and proximity to T_g are considered, implying the influence of non-covalent interactions is also important at high rates.

An expanded plot of KE_{50} for all the ENB/DCPD and HDMN/DCPD copolymers is provided along with visual analysis of selected failed specimens in Figure 8. The room temperature KE_{50} measurements (all data in Figure 8A except the pink points) revealed that high $M_{c,a}$ values generally resulted in better performance during a high rate impact event. Figure 8B shows that

28

KE_{50} follows a linear dependence on $1/M_{c,ar}$, reminiscent of the T_g dependence shown in Figure

4B. Modifying Equation 2 slightly for KE_{50} , we obtain

$$KE_{50} = KE_{50,\infty} - \frac{K}{M_c} \quad 3$$

This equation yields a material specific parameter, K , of 407 ± 24 , and a limiting KE_{50} (KE_{50} at an infinite unentangled molecular weight) of 4.3 ± 0.1 . The K parameter may be related to the fractional free volume of a material. The limiting KE_{50} value of 4.3 ± 0.1 is slightly greater than that of pENB, which is 3.98 ± 0.1 . This analysis suggests that pENB is very close to the maximum high rate impact performance possible for the ROMP system, as large increases in molecular weight between crosslinks (or reduced entanglements in the case of pENB) will only yield fractional increases in the normalized KE_{50} .

29

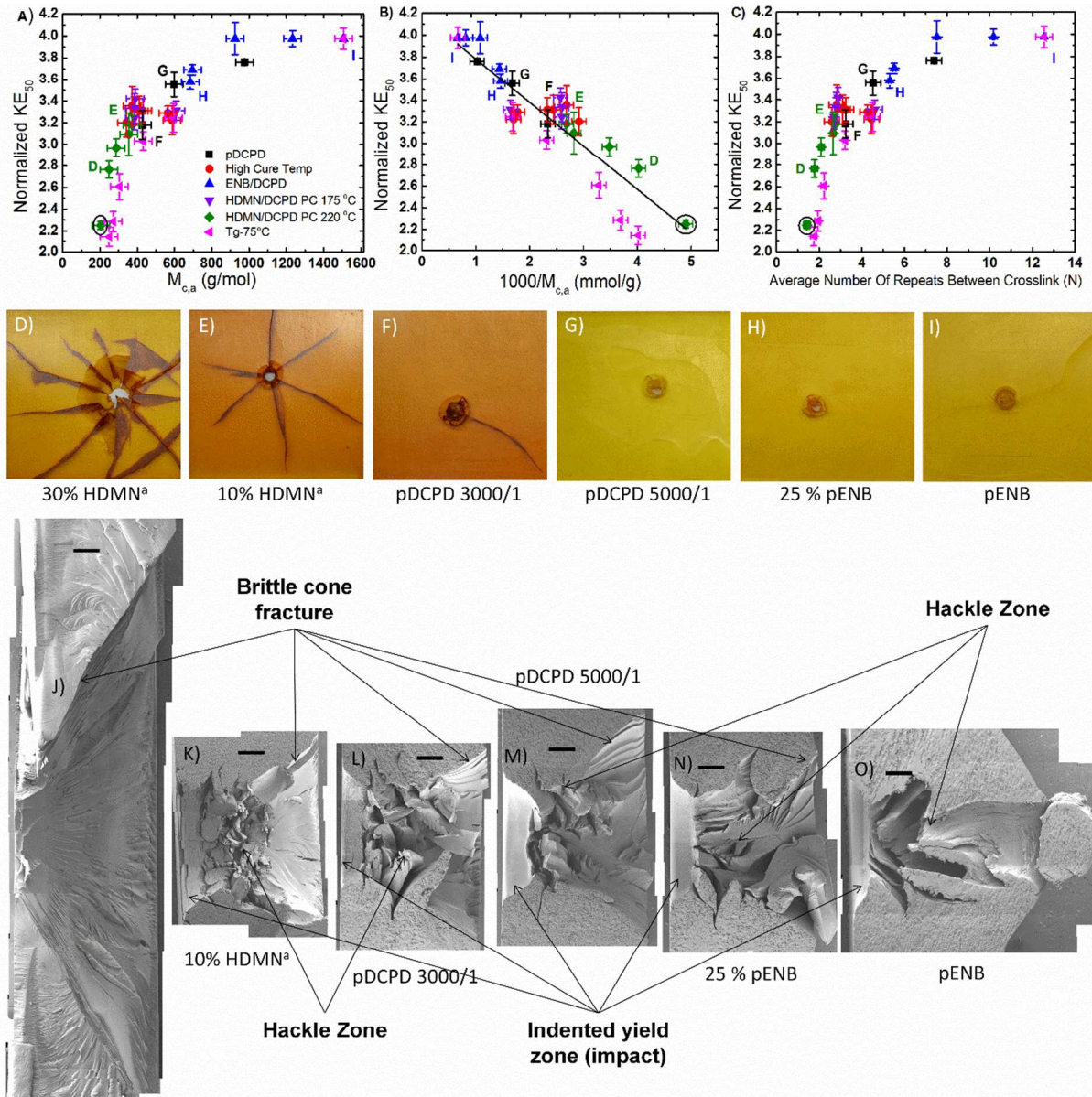


Figure 8. The relationship between A) normalized KE_{50} and $M_{c,a}$ for the pDCPD post-cured higher temperature (black), the ENB/DCPD copolymers (red), the series of HDMN/DCPD copolymers post-cured at 175 °C and a 5000/1 catalyst loading (blue), and the series of HDMN/DCPD copolymers post-cured at 220 °C and a 3000/1 catalyst loading (green). B) Normalized KE_{50} as a function of $1000/M_{c,a}$. The solid line is a fit of Equation 3 to the data. The circled data point in A-C is the only sample that failed due to spalling rather than projectile penetration (i.e., the 40% HDMN formulation). C) Normalized KE_{50} versus the average number of repeats between crosslinks is shown in (A-C). D-I) photographs of representative samples showing transition in failure morphology corresponding to labels in (A-C). J-O) Composite SEM images of penetrated cross-sections for samples D-I (in the same order as D-I, projectile entered from the left side of each image). The composite images consist of multiple SEM images stitched together. All scale bars are 1 mm.

Figure 8C shows normalized KE_{50} as a function of the average number of segments between crosslinks (N). The trend is continuous, but the KE_{50} begins to transition from an essentially

30

$M_{c,a}$ -independent regime to one in which there is a strong dependence on the chain length between crosslinks below an N value of about 6. This result is interesting in the context of the strong T_g dependence on $M_{c,a}$ below 6 repeat units shown in Figure 4.

3.4 Mechanism of failure at high rate

The mechanism of failure during the KE_{50} measurement also changed with $M_{c,a}$. Three types of damage to the polymer were visually observed following the work of Bain et al.⁶ (see Figures S4 and S5 in the supplemental information). The first type of damage was plastic deformation, in which the target macroscopically yields under the imposed stress of the projectile. This can be observed in the photograph of pENB in Figure 8I. Radial fracture is the second type of damage, in which cracks initiating at the back face ahead of the projectile propagate through the plate thickness toward the front face and radially out from the impact site. This type of damage is observed in Figure 8D to F. The third type of damage is cone cracks, in which Hertzian cone fracture allows the kinetic energy of the projectile to transfer to and expel fragments of polymeric material (i.e., spall) directly behind the impact site into the witness as observed in Figure 8D and Figure S5. It is important to note that, in brittle failure, spall fragments formed by cone cracks (rather than the projectile itself) can penetrate the witness foil causing failure in the high rate test. However, this was observed for only one sample in this study (40% HDMN, circled in Figure 8A to C).

Figure 8J to O show SEM images of cross-sections from selected samples penetrated at KE_{50} . At low $M_{c,a}$ (Figure 8J, corresponding to the photo in Figure 8D), the sample shows no front face plastic indentation at impact. Rather, fully brittle cone fracture exhibiting a very wide cone

31

angle was observed. At intermediate values of $M_{c,a}$ (Figure 8K to N, corresponding respectively to the photos in Figure 8E to H), a mixed failure mode was observed with a plastically indented impact zone on the front face of the sample followed by artifacts of plastic deformation (hackles) in the middle and a brittle cone fracture at the back half of the specimen. The plastic deformation artifacts tend to increase in intensity with increasing $M_{c,a}$. For 25% PENB (Figure 8N), there is a slight bulge around the exit hole at the back face of the specimen. At the highest $M_{c,a}$ (Figure 8O), the failure is purely ductile and the back face bulge is pronounced due to significant plastic deformation.

Previous work and the data in Figure 7 suggest that the failure mechanism during a high rate impact event is dependent on both fracture toughness K_{IC} , which influences Hertzian cone crack initiation for brittle materials, and the rate-dependent yield stress, which influences failure of materials that plastically deform at the impact site.^{6, 72, 73} Figure 9A compares the data from this study with the models developed previously⁶, one of which is the Hertzian cone initiation energy (blue solid line) based on the following equation:

$$V_C \approx \frac{950K_{IC}^{5/3}}{R\rho_1^{1/2}E^{*7/6}} \quad 4$$

Here, V_C is the critical velocity for cone crack initiation, R is the projectile radius, the subscripts 1 and 2 designate the projectile and target, respectively, and the reduced Young's Modulus $E^* \approx \frac{E_2}{1-\nu_2^2}$. We assumed a Poisson's ratio ν of 0.35 for all target materials in this study. The KE_{50}

values measured at room temperature for the samples with low K_{IC} values (20%, 30% and 40%

32

HDMN) were close to the Hertzian cone fracture model prediction (blue line in Figure 9A). The differences between the data and model are consistent with the excess energy needed to eject the cone fragment and penetrate the witness foil⁶. Samples with higher K_{IC} deviate from Equation 4, consistent with previous observations in which a transition from Hertzian cone-dominated failure to yield-dominated failure was observed with increasing K_{IC} of epoxies⁶. The yield-dominated failure model (multiplied by a factor 3.8 which empirically accounts for rate dependence as described in ⁶) is:

$$V_Y \approx 3.8 * 3\sigma_{Y,2} \left[\frac{(1 - 2\nu_2)(1 + \nu_2)}{\rho_2(1 - \nu_2)E_2} \right]^{1/2} \quad 5$$

Here, V_Y is the critical velocity for cone crack initiation. This model is adopted from the finite element models of Compton et al.⁷² and depends on σ_Y and E measured at room temperature (black dotted line in Figure 9A) and at $T_g-75^\circ\text{C}$ (red dashed line in Figure 9A). As shown in Figure 9A, the predictions of Equation 5 are quite different for room temperature (black line), which has a weakly negative slope as a function of K_{IC} , and $T_g-75^\circ\text{C}$ (red dashed line), which has a stronger positive slope. While Equation 5 is not an explicit function of K_{IC} , it is a linear function of yield stress, which is related to T , $M_{c,a}$ and K_{IC} (see Figure 5C-D and Figure S3B in the supplementary information). Figure 5E shows that K_{IC} is a nearly linear function of $M_{c,a}$ for all temperature conditions, and Figure 5C shows that yield stress decreases weakly with $M_{c,a}$ at room temperature and increases with $M_{c,a}$ at $T_g-75^\circ\text{C}$. These trends mirror the predictions of Equation 5 in Figure 9A (a weak decrease at room temperature, a stronger increase at $T_g-75^\circ\text{C}$), demonstrating the dominant effect of yield stress in this model.

33

Equation 5 fits the $T_g-75^\circ\text{C}$ (red) data remarkably well, which indicates that the ROMP polymers are in a regime of ductile failure dominated by yielding at $T_g-75^\circ\text{C}$. However, the yield model tends to overpredict KE_{50} at room temperature (black data). As shown in Figure 9B, this overprediction is a systematic function of $T-T_g$. These model results suggest that a gradual transition in failure mode occurs for the ROMP series with changing $M_{c,a}$, from purely brittle to mixed ductile/brittle to purely ductile, consistent with the observations in Figure 8. This is in contrast to epoxy resins, which generally exhibit a brittle failure mechanism with substantial cracking upon ballistic impact unless they are relatively close to their T_g (see Figure S6 and the corresponding discussion in the supplemental information).⁴⁷

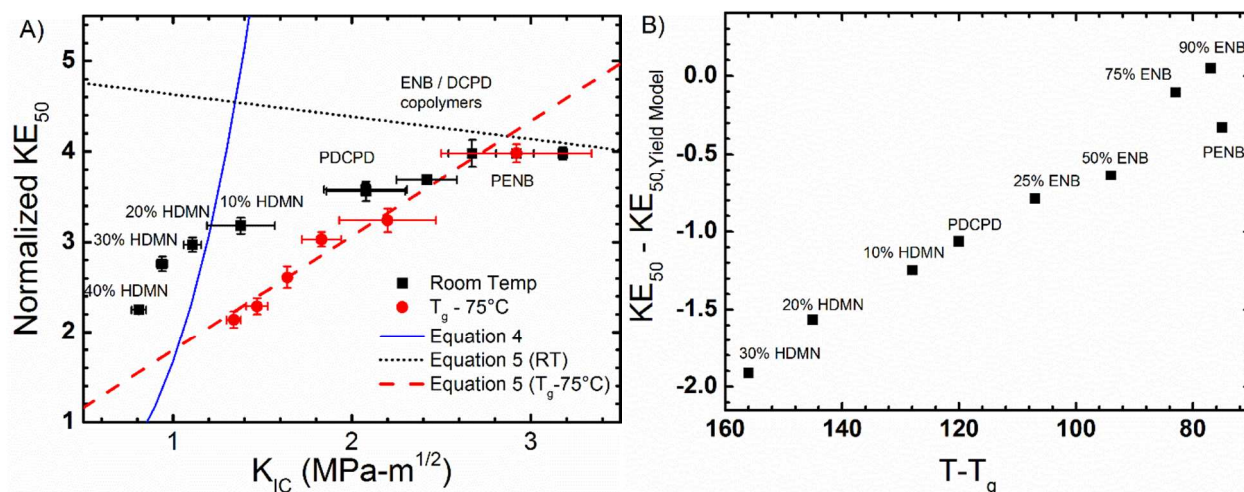


Figure 9. A) KE_{50} of ROMP resins as a function of K_{IC} compared with failure models described in ⁶. Note that the black dotted and red dashed curves are linear fits to discrete predictions of Equation 5 based on the quasi-static tensile data reported in Table 2. B) Deviation of room temperature KE_{50} from the yield model prediction plotted as a function of $T-T_g$.

3.5 Molecular dynamics simulation results

The experimental results above show that the behavior of ROMP systems is unique compared to thermosets with stronger non-covalent interactions. In an effort to understand what influences the ROMP mechanical properties at a molecular level, we employed MD simulations

34

to study the influence of $M_{c,a}$ and chain rigidity on molecular mobility in ROMP resins. We previously hypothesized that the high toughness and ballistic performance of pDCPD compared to networks with polar constituents (i.e., epoxy-amine based thermosets) stemmed from differences in nanovoid formation and growth.^{9, 18} We found that, for networks with a similar M_c , the use of chains with stiff, bulky monomers (that packed poorly) or weaker non-covalent interactions encouraged nanovoid formation. In contrast, higher chain flexibility or higher polarity suppressed nanovoid formation. We also found that MD simulations were able to correctly predict qualitative changes in glassy modulus, rubbery modulus, and yield stress for thermosets of different chemical compositions¹⁸. Here, we focused on the role of M_c in nanovoid formation and its potential influence on the mechanical properties of ROMP resins.

We previously showed the mobility of the four-functional crosslink sites in pDCPD to be highly restricted relative to other monomers.¹⁰ As such, increasing the density of crosslink junctions will frustrate the local packing of monomers and potentially alter the nanovoid content. To test this hypothesis, molecular structures of crosslinked pDCPD were created with varying M_c (including linear, uncrosslinked pDCPD) and deformed with high-strain-rate uniaxial extension in the context of MD simulations. The prevalence of nanoscale voids was measured during the deformation of each network. As an additional reference, we compared the pDCPD results with the linear polymer pENB, which had the overall highest experimental K_{IC} and KE_{50} .

35

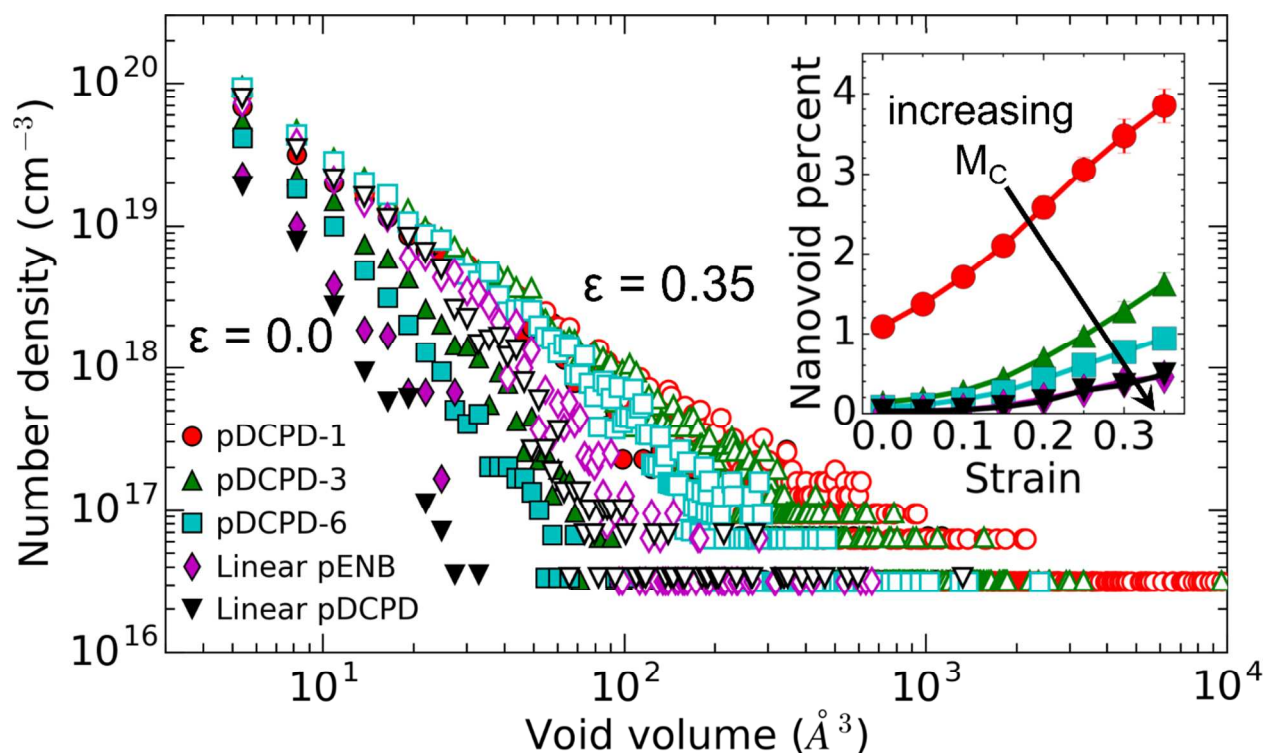


Figure 10. Histograms of nanovoid volumes in pDCPD and pENB undergoing uniaxial extension deep in the glassy state (150 K) at 0% (solid symbols) and 35% (open symbols) engineering strain. Inset shows the nanovoid volume percent, i.e., the percent of the simulation box volume occupied by nanovoids.

The nanovoid content can be represented as a histogram of void number density as a function of nanovoid volume (Figure 10). These distributions demonstrate the wide range of sizes of nanovoids that can form (from $\sim 1 \text{ \AA}^3$ to over 10000 \AA^3), depending on loading condition and M_c . The effects of these factors are most easily visualized as the nanovoid volume percent (inset in Figure 10). The effect of applied strain is to increase the nanovoid volume percent, because the Poisson's ratio is less than 0.5 at this temperature and strain rate. This behavior is consistent with our expectations based on fundamental material properties and our previous simulations.^{10, 18} The effect of crosslink density, which is most evident at high strain, is more interesting; that is, decreasing M_c increases the nanovoid volume percent. Thus, the polymer with the lowest M_c , pDCPD-1 ($M_c=198 \text{ g/mol}$), has the highest nanovoid volume percent,

36

followed in decreasing order by pDCPD-3 ($M_c=463$ g/mol), pDCPD-6 ($M_c=859$ g/mol), and the linear polymers. Previous simulations and experiments showed that rigid molecules frustrate polymer packing, leading to an increase in nanovoid content.^{18, 74-77} Intuitively, one would expect that more rigid systems would be forced to accommodate strain by void formation, while less rigid systems would have the flexibility to accommodate strain between chains via intermolecular spacing that would be smaller than the nanovoids defined herein. As such, we attempted to quantify the rigidity of these systems to explain the results obtained in Figure 10 and determine if these can be correlated with the experimental work above.

One way to quantify flexibility is to define angles along the polymer backbone (Figure 11A) and observe the distribution of these angles (Figure 11B). A wider distribution (larger standard deviation, σ) indicates flexibility, whereas a narrower distribution indicates rigidity.^{18, 78} We found that crosslinked pDCPD (i.e., pDCPD-3 and pDCPD-6), linear pDCPD and pENB have similar distributions ($\sigma \approx 24^\circ$ to 26°). Previously, we used this metric to distinguish amine-based crosslinkers as rigid ($\sigma \approx 10^\circ$) or flexible ($\sigma \approx 30^\circ$).¹⁸ The angle distributions of the ROMP polymers are similar, so their flexibility is essentially identical by this measure and are similar to the relatively flexible polypropylene oxide amine-based crosslinkers studied previously in epoxy systems¹⁸.

37

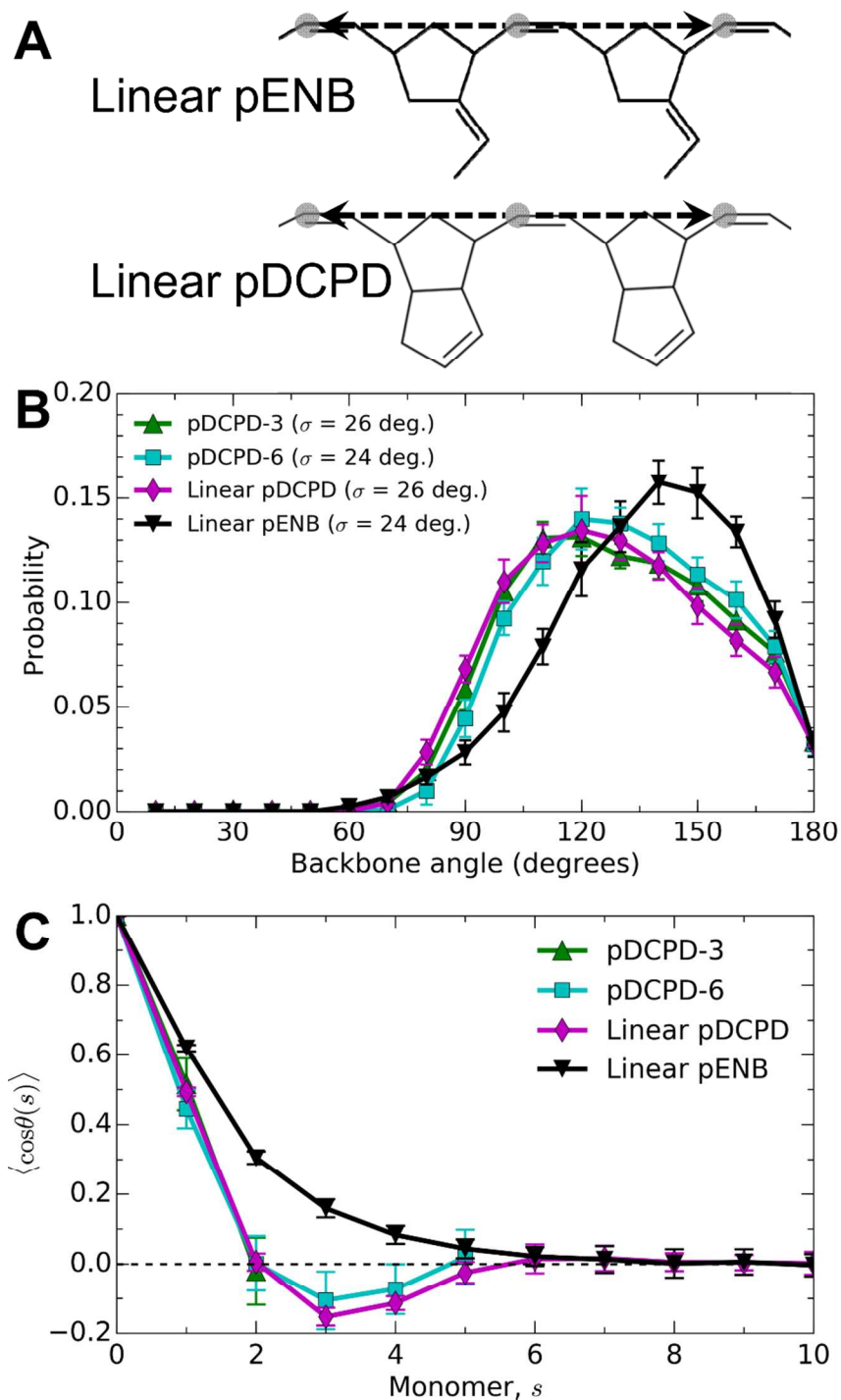


Figure 11. Flexibility of linear pDCPD and pENB. A) Diagram of atoms used to define vectors for calculating backbone angles and orientational correlation. B) Probability distribution of backbone angles. The standard deviation of the distribution, σ , shown in the legend is a measure of flexibility. C) Orientational correlation of the backbone. Error bars are the standard deviation of the mean of 10 sets of polymer conformations.

38

Another widely used method to describe the intrinsic rigidity of polymers is the wormlike chain (WLC) model, wherein the orientational correlation of the polymer backbone decays exponentially.⁷⁹ The decay is expressed as $\langle \cos \theta(s) \rangle = \exp(-s/L_p)$, where θ is the angle between the first monomer and monomer s , L_p is the persistence length, and the angle brackets indicate ensemble averaging. We used the vectors shown in Figure 11A to define the backbone orientation at each monomer, and the results are shown in Figure 11C. Note that the data for pDCPD-3 ($M_c=463$ g/mol) stops at $s=2$ and the data for pDCPD-6 ($M_c=859$ g/mol) stops at $s=5$ because a crosslink exists at the next monomer. The negative correlations for pDCPD in Figure 11C are because the bulky side groups in pDCPD cause steric repulsion between neighboring monomers, inducing a slight helical or zigzag conformation, which still indicates orientational correlation. As shown in Figure 11C, the orientational correlation drops below zero before returning to zero for linear pDCPD, and the same trend is followed regardless of the M_c (i.e., the pDCPD-3, pDCPD-6 and linear data all follow the same trend until the data end just before a crosslink point). The persistence lengths of the linear polymers were obtained from a fit of the data in Figure 11C and were similar for linear pENB and linear pDCPD ($s \sim 1-2$ monomers, or $\sim 5-10$ Å). These values were also similar for crosslinked pDCPD with either 3 (pDCPD-3) or 6 (pDCPD-6) monomers between crosslinking junctions. The persistence length is a fit parameter, and it does not indicate where orientational correlation is lost. This information can be obtained from Figure 11C, which shows that polymer rigidity (as evidenced by orientational correlation) changes continuously and is lost as the M_c increases beyond an equivalent of 5 monomers, or about 660 g/mol for pDCPD (i.e., above pDCPD-3 and below pDCPD-6) and about 600 g/mol for pENB. This indicates that pDCPD-3 is relatively more rigid than either pDCPD-6 or

39

linear pDCPD. Interestingly, these results are similar to the $M_{c,a}$ (about 400 g/mol) at which measured K_{IC} and G_{IC} data for ROMP polymers diverge from that of the polar polymers in Figure 5G and H. They are also similar to the range in which the slope of the KE_{50} vs. $M_{c,a}$ plot changes significantly in Figure 8C.

Thus, the trend of increasing nanovoid volume percent with decreasing M_c (Figure 10) can be explained as follows. Crosslinking results in increasing rigidity as the linear molecular segments between crosslinks become shorter and stiffer. Similarly, the motion of the chain ends is increasingly restricted with increased crosslink density. The linear segments in pDCPD-1 are highly rigid because their lengths are comparable to the persistence length, while linear segments in pDCPD-3 are somewhat rigid as their lengths are larger than the persistence length but smaller than the lengths where orientational correlation is lost. As the linear segments increase in length, their rigidity decreases, approaching that of the linear polymers. Accordingly, nanovoids are most prevalent in pDCPD-1 ($M_c=198$ g/mol, the most rigid and least able to accommodate strain without void formation) and least prevalent in the linear polymers (the most flexible and most able to accommodate strain without void formation). Furthermore, the near-identical flexibility of pENB and linear pDCPD is consistent with their similar void content.

The simulations performed here show that although density is reduced by increasing M_c (which agrees with experimental data in Table 1), the nanovoid fraction actually decreases (Figure 10). This result indicates that increasing M_c redistributes the unoccupied volume from relatively large contiguous voids into smaller interstitial spaces between chains (“free volume”), which should (and do) correspond to a reduced glass transition temperature. Changes in free volume

40

from MD calculations are illustrated in the supplemental information, which shows that pENB has a higher change in volume during strain than pDCPD (Figure S7).

Taken together, the experiments and simulations correlate increases in M_c with increases in the fracture toughness, KE_{50} , and interstitial space (i.e., “free volume”). We postulate that interstitial space can enhance energy dissipation by increasing the accessible volume available for chains to rearrange or slide past each other during deformation. Thus, the reduction in nanovoid content with increasing M_c seems to be beneficial, especially if it reflects a redistribution of the unoccupied volume on finer length-scales that allows relative motion between chains. The positive correlation between free volume and chain mobility is well-established.⁵⁰ Here, we postulate that the increased mobility allows for increased toughness and the plastic deformation observed at high values of M_c during high rate impact testing. Additionally, experimental observations of the volume change and surface morphology in necked regions of uniaxial tensile samples reveal an apparent tendency to form craze-like flaws with increasing M_c (Figures S8 - S10 in the supplementary information), suggesting increased mobility associated with increasing M_c may ultimately lead to formation of larger scale voids, which both contribute to and limit plastic deformation.

41

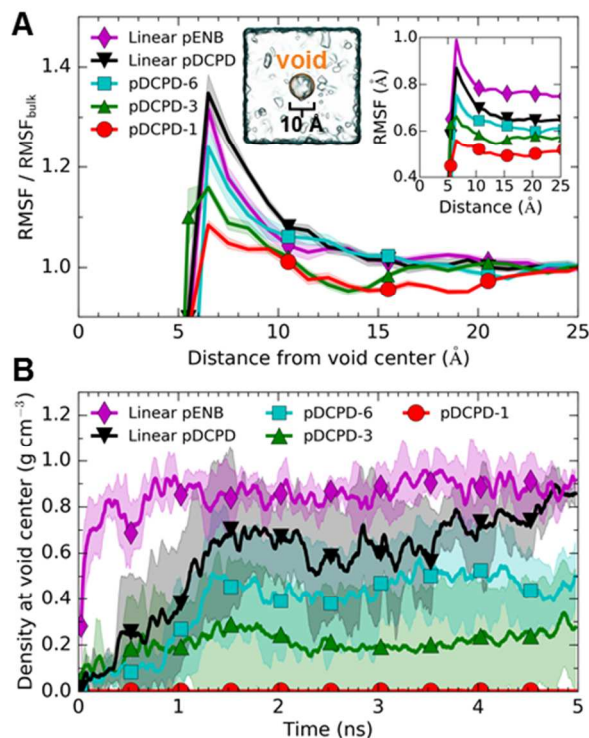


Figure 12. A) Mobility of atoms near a void, normalized by the bulk atomic mobility. Inset diagram demonstrates the large predefined void (sphere with diameter 10 Å, with a volume of $\sim 500 \text{ \AA}^3$) surrounded by the polymer (density isosurface). The void was held open by a repulsive spherical probe. Inset plot shows non-normalized atomic mobility. The root-mean-square fluctuation (RMSF) was calculated over time periods of 10 ps during a 5 ns simulation at 300 K. The 10 ps time period allowed us to collect a large number of independent samples, and we have previously shown that qualitative trends are independent of the sampling period.¹⁰ Shaded regions show the standard deviation of a 10 block average. B) Relaxation capability of the polymer near a void. After removing the repulsive sphere maintaining the void, the density within the void region was followed over time. The time required to collapse the void (i.e., reach bulk density $\approx 0.9 \text{ g cm}^{-3}$) is a measure of how quickly the polymer can plastically relax. The simulated T_g values of all polymers were $\sim 450 \text{ K}$, except for pDCPD-1, which has a very high T_g .¹⁰ The temperature for these simulations (400 K) is below the simulated T_g of all polymers, but is high enough to accelerate the collapse process. Lines and shaded regions are the average and standard deviation, respectively, of 5 simulations initialized with different velocities. The standard deviation is large because void collapse is a thermally activated process, akin to bubble nucleation or droplet condensation, so the time-to-collapse is stochastic.

The connection between interstitial space, mobility, and plasticity were investigated by constructing polymer models containing a large predefined void (inset Figure 12A). First, we examined the mobility around this void. As in previous work,¹⁰ we quantified mobility as the root-mean-square fluctuation (RMSF) of each atom around its average position over a period of time. We averaged the atomic mobility as a function of distance from the center of the void, where the void space was maintained by a repulsive spherical probe. Four interesting findings

42

are apparent. (1) Mobility is highest near the void and decays to the bulk value over ~ 1 nm for all polymers (Figure 12A). (2) The mobility near the void increases with increasing M_c . (3) The bulk mobility increases with increasing M_c (inset Figure 12A). (4) The bulk mobility is higher in pENB than in linear pDCPD. Higher mobility near the void supports the idea that unoccupied volume locally increases chain mobility. The increased mobility near the void and in the bulk with increasing M_c supports the idea that increased free volume enables greater chain mobility. The higher bulk mobility in pENB further suggests that it may have a greater capability for plastic deformation than linear pDCPD.

Next, we examined the ability of the polymer near a void to relax over time. We quantified this as the time needed for the void to collapse following the removal of the spherical probe that had been holding it open (Figure 12B). After removing this support, the polymer must deform plastically to fill the empty space. We monitored this process by recording the density near the former location of the probe. The void was deemed to have collapsed once the region reached the bulk density ($\sim 0.9 \text{ g cm}^{-3}$). The density in pDCPD-1 shows no change over 5 ns, indicating no relaxation. In contrast, in pENB the density plateaus within 0.5 ns, indicating that the polymer rapidly relaxes to fill the void. Linear pDCPD reaches bulk density over ~ 5 ns, indicating a more gradual relaxation. The remaining cross-linked polymers, pDCPD-3 ($M_c=463 \text{ g/mol}$) and pDCPD-6 ($M_c=859 \text{ g/mol}$), lie between pDCPD-1 ($M_c=198 \text{ g/mol}$) and linear pDCPD in order of increasing M_c . Interestingly, faster relaxation times (Figure 12B) correspond to higher atomic mobility (Figure 12A), which in turn corresponds to increased M_c . This finding is reasonable but was not *a priori* guaranteed, because side chain motions may increase atomic mobility without necessarily accelerating segmental relaxations.

43

These results suggest the following picture. Glassy polymers, having a Poisson's ratio < 0.5 , must form voids to accommodate volume increases during deformation. In the early stages of deformation, these are likely nanoscale unoccupied volumes rather than macroscopic holes. For resins with lower M_c , this unoccupied volume is consolidated into relatively large nanovoids. Chain mobility is low, so there is no mechanism to relax stress concentrated near these voids. As strain increases, the voids cannot grow or deform, so the chains are pulled taut and break, causing embrittlement. In resins with higher M_c , the unoccupied volume is distributed across small interstitial spaces, allowing greater chain mobility. In fact, the relative absence of large, stress-concentrating nanovoids in high- M_c resins may be because relaxation of the polymer happens on roughly the same time scale as nanovoid growth; however, a more detailed study is necessary to fully quantify the relative timescales of segmental relaxation and void formation/growth under various conditions. In any case, the chains can deform to dissipate stress concentrations, ultimately leading to yielding processes that improve ductility. Furthermore, the weak interchain interactions also facilitate mobility, relaxation, and ductility. Strong interactions have been shown to increase interchain friction,⁸⁰ which would decrease mobility. This effect would contribute to the differences between pDCPD/pENB (weak nonpolar interactions, ductile) and, for example, epoxy-based resins (strong polar interactions, brittle).

4. Conclusion

In this work, we systematically investigated the influence of molecular weight between crosslinks on quasi-static and high rate impact performance of ROMP-based polymer systems. These polymers offered an ideal system for evaluating the influence of crosslink density on physical properties such as quasi-static fracture toughness and high rate impact because the

44

$M_{c,a}$ can be easily controlled and they lack strong non-covalent interactions that would act as apparent crosslinking points. Our relevant conclusions are as follows:

- We synthesized a range of ROMP resins with T_g values as high as 178 °C. The T_g was proportional to $1/M_{c,a}$ for the ROMP resins.
- The quasi-static mechanical properties (modulus, tensile yield strength, K_{IC} and G_{IC}) of the ROMP resins were compared with more polar thermosets having strong non-covalent interactions. The moduli and tensile yield strengths of the ROMP resins were lower, while the K_{IC} and G_{IC} were 2 to 3 times higher and the high rate impact resistance was 3 to 5 times higher than polar resins at comparable values of $M_{c,a}$ and $T-T_g$. Taken together, these results imply that the lack of strong non-covalent interactions in the ROMP resins led to significantly greater toughness as a function of $M_{c,a}$ and distance from T_g compared to more polar thermosets.
- The high rate impact performance of the resins measured at T_g-75 °C showed a clear dependence on the yield stress, following a ductile failure model previously developed for rubber-toughened epoxies. Room temperature high rate data showed reasonable agreement with the brittle Hertzian cone fracture-dominated failure (which is a function of fracture toughness and modulus) at low $M_{c,a}$ and reasonable agreement with the ductile failure model at high $M_{c,a}$ values. This transition from one model to another corresponded to a gradual brittle to ductile transition observed in SEM images of the high rate impact specimens.
- MD simulation results provided four primary conclusions: (i) nanovoid content and nanovoid volume increase with decreasing M_c , (ii) orientational correlation for the

polymers shows a continuous transition from high correlation for near repeat units to low correlation for monomers greater than about 5 repeat units away, (iii) the persistence length of linear pDCPD and pENB were 1-2 monomers, and (iv) molecular mobility in the bulk polymer and near voids increases with increasing M_c . All these observations suggest that high M_c formulations should be more capable of plastic deformation than low M_c formulations. This conclusion is consistent with the quasi-static K_{IC} and G_{IC} value dependence on $M_{c,a}$ and the gradual transition from ductile to brittle failure in high rate KE_{50} that occurred as a function of $M_{c,a}$. These result suggests that, in the absence of strong non-covalent interactions, the rigidity of the system has a strong influence on the mechanical properties.

These conclusions illustrate that the $M_{c,a}$ in a model system having few non-covalent interactions has a profound effect on both atomistic-scale behavior and bulk mechanical properties. These conclusions provide critical insight into polymer systems and can be used to engineer polymers at a molecular level to obtain the desired physical properties for various applications.

5. References

1. A. Arnebold, S. Wellmann and A. Hartwig, *Polymer*, 2016, **91**, 14-23.
2. K. A. Masser, D. B. Knorr Jr, M. D. Hindenlang, J. H. Yu, A. D. Richardson, K. E. Strawhecker, F. L. Beyer and J. L. Lenhart, *Polymer*, 2015, **58**, 96-106.
3. H. Abdollahi, A. Salimi and M. Barikani, *Journal of Applied Polymer Science*, 2016, **133**.
4. E. Bugnicourt, J. Galy, J. F. Gerard and H. Barthel, *Polymer*, 2007, **48**, 1596-1605.
5. L. M. McGrath, R. S. Parnas, S. H. King, J. L. Schroeder, D. A. Fischer and J. L. Lenhart, *Polymer*, 2008, **49**, 999-1014.
6. E. D. Bain, D. B. Knorr, A. D. Richardson, K. A. Masser, J. Yu and J. L. Lenhart, *Journal of Materials Science*, 2016, **51**, 2347-2370.
7. E. R. Mafi and M. Ebrahimi, *Polymer Engineering and Science*, 2008, **48**, 1376-1380.

46

8. E. Bittmann and G. W. Ehrenstein, *Angewandte Makromolekulare Chemie*, 1998, **258**, 93-98.
9. D. B. Knorr Jr, K. A. Masser, R. M. Elder, T. W. Sirk, M. D. Hindenlang, J. H. Yu, A. D. Richardson, S. E. Boyd, W. A. Spurgeon and J. L. Lenhart, *Composites Science and Technology*, 2015, **114**, 17-25.
10. R. M. Elder, J. W. Andzelm and T. W. Sirk, *Chemical Physics Letters*, 2015, **637**, 103-109.
11. L. Leibler, M. Rubinstein and R. H. Colby, *Macromolecules*, 1991, **24**, 4701-4707.
12. M. Rubinstein and A. N. Semenov, *Macromolecules*, 2001, **34**, 1058-1068.
13. K. Yamauchi, J. R. Lizotte, D. M. Hercules, M. J. Vergne and T. E. Long, *Journal of the American Chemical Society*, 2002, **124**, 8599-8604.
14. R. P. Sijbesma, F. H. Beijer, L. Brunsveld, B. J. B. Folmer, J. H. K. K. Hirschberg, R. F. M. Lange, J. K. L. Lowe and E. W. Meijer, *Science*, 1997, **278**, 1601-1604.
15. D. W. R. Balkenende, C. A. Monnier, G. L. Fiore and C. Weder, *Nature Communications*, 2016, **7**, 10995.
16. D. W. R. Balkenende, R. A. Olson, S. Balog, C. Weder and L. Montero de Espinosa, *Macromolecules*, 2016, **49**, 7877-7885.
17. C. B. St.Pourcain and A. C. Griffin, *Macromolecules*, 1995, **28**, 4116-4121.
18. R. M. Elder, D. B. Knorr, J. W. Andzelm, J. L. Lenhart and T. W. Sirk, *Soft Matter*, 2016, **12**, 4418-4434.
19. E. D. Crawford and A. J. Lesser, *Polymer Engineering and Science*, 1999, **39**, 385-392.
20. E. Crawford and A. J. Lesser, *Journal of Polymer Science Part B-Polymer Physics*, 1998, **36**, 1371-1382.
21. L. Plangsangmas, J. J. Mecholsky and A. B. Brennan, *Journal of Applied Polymer Science*, 1999, **72**, 257-268.
22. F. FernandezNograro, A. Valea, R. LlanoPonte and I. Mondragon, *European Polymer Journal*, 1996, **32**, 257-266.
23. K. Cho, D. Lee and C. E. Park, *Polymer*, 1996, **37**, 813-817.
24. J. P. Bell, *Journal of Applied Polymer Science*, 1970, **14**, 1901-&.
25. C. Y. Li and A. Strachan, *Polymer*, 2015, **75**, 151-160.
26. E. L. Dias, S. T. Nguyen and R. H. Grubbs, *Journal of the American Chemical Society*, 1997, **119**, 3887-3897.
27. C. W. Bielawski and R. H. Grubbs, *Progress in Polymer Science*, 2007, **32**, 1-29.
28. T. M. Trnka and R. H. Grubbs, *Accounts of Chemical Research*, 2001, **34**, 18-29.
29. M. S. Sanford, J. A. Love and R. H. Grubbs, *Journal of the American Chemical Society*, 2001, **123**, 6543-6554.
30. X. Liu, J. K. Lee, S. H. Yoon and M. R. Kessler, *Journal of Applied Polymer Science*, 2006, **101**, 1266-1272.
31. X. Sheng, M. R. Kessler and J. K. Lee, *Journal of Thermal Analysis and Calorimetry*, 2007, **89**, 459-464.
32. T. C. Mauldin, K. Haman, X. Sheng, P. Henna, R. C. Larock and M. R. Kessler, *Journal of Polymer Science Part A: Polymer Chemistry*, 2008, **46**, 6851-6860.
33. X. Sheng, J. K. Lee and M. R. Kessler, *Polymer*, 2009, **50**, 1264-1269.
34. W. Jeong and M. R. Kessler, *Carbon*, 2009, **47**, 2406-2412.
35. S. Bhuyan, S. Sundararajan, X. Sheng and M. Kessler, *Wear*, 2011, **270**, 550-554.

47

36. M. R. Kessler and S. R. White, *Journal of Polymer Science Part A: Polymer Chemistry*, 2002, **40**, 2373-2383.
37. T. C. Mauldin and M. R. Kessler, *Journal of Thermal Analysis and Calorimetry*, 2009, **96**, 705-713.
38. M. R. Kessler, G. E. Larin and N. Bernklau, *Journal of Thermal Analysis and Calorimetry*, 2006, **85**, 7-12.
39. E. Richaud, P. Y. Le Gac and J. Verdu, *Polymer Degradation and Stability*, 2014, **102**, 95-104.
40. G. M. Odegard, B. D. Jensen, S. Gowtham, J. Wu, J. He and Z. Zhang, *Chemical Physics Letters*, 2014, **591**, 175-178.
41. G. Yang, T. C. Mauldin and J. K. Lee, *RSC Advances*, 2015, **5**, 59120-59130.
42. A. Hejl, O. A. Scherman and R. H. Grubbs, *Macromolecules*, 2005, **38**, 7214-7218.
43. P. v. R. W. Schleyer, James Earl, Jr.; Blanchard, K. R., *Journal of the American Chemical Society*, 1970, **92**, 2377-2389.
44. U. S. D. o. Defense, *Journal*, 1997.
45. G. J. Czarnecki, *Composites Part B-Engineering*, 1998, **29**, 321-329.
46. E. P. Gellert, S. J. Cimpoeu and R. L. Woodward, *International Journal of Impact Engineering*, 2000, **24**, 445-456.
47. D. B. Knorr, Jr., J. H. Yu, A. D. Richardson, M. D. Hindenlang, I. M. McAninch, J. J. La Scala and J. L. Lenhart, *Polymer*, 2012, **53**, 5917-5923.
48. M. C. M. van der Sanden and H. E. H. Meijer, *Polymer*, 1993, **34**, 5063-5072.
49. A. J. Lesser and E. Crawford, *Journal of Applied Polymer Science*, 1997, **66**, 387-395.
50. T. G. Fox Jr and P. J. Flory, *Journal of Applied Physics*, 1950, **21**, 581-591.
51. T. G. Fox and P. J. Flory, *Journal of Polymer Science*, 1954, **14**, 315-319.
52. K. A. Masser, D. B. Knorr, J. H. Yu, M. D. Hindenlang and J. L. Lenhart, *Journal of Applied Polymer Science*, 2016, **133**, n/a-n/a.
53. R. Rahul and R. Kitey, *Composites Part B-Engineering*, 2016, **85**, 336-342.
54. J. Liu, H.-J. Sue, Z. J. Thompson, F. S. Bates, M. Dettloff, G. Jacob, N. Verghese and H. Pham, *Polymer*, 2009, **50**, 4683-4689.
55. H. J. Sue, P. M. Puckett, J. L. Bertram, L. L. Walker and E. I. Garcia-Meitin, *Journal of Polymer Science Part B: Polymer Physics*, 1999, **37**, 2137-2149.
56. W. J. Boo, L. Sun, J. Liu, E. Moghbelli, A. Clearfield, H.-J. Sue, H. Pham and N. Verghese, *Journal of Polymer Science Part B: Polymer Physics*, 2007, **45**, 1459-1469.
57. R. A. Pearson and A. F. Yee, *Journal of Materials Science*, 1989, **24**, 2571-2580.
58. J. Ma, M.-S. Mo, X.-S. Du, P. Rosso, K. Friedrich and H.-C. Kuan, *Polymer*, 2008, **49**, 3510-3523.
59. T. H. Hsieh, A. J. Kinloch, K. Masania, A. C. Taylor and S. Sprenger, *Polymer*, 2010, **51**, 6284-6294.
60. I. M. McAninch, G. R. Palmese, J. L. Lenhart and J. J. La Scala, *Journal of Applied Polymer Science*, 2013, **130**, 1621-1631.
61. S. Deng, L. Ye and K. Friedrich, *Journal of Materials Science*, 2007, **42**, 2766-2774.
62. C. L. Sherman, R. C. Zeigler, N. E. Verghese and M. J. Marks, *Polymer*, 2008, **49**, 1164-1172.

48

63. M. Franco, M. A. Corcuera, J. Gavaldà, A. Valea and I. Mondragon, *Journal of Polymer Science Part B: Polymer Physics*, 1997, **35**, 233-240.
64. A. J. Lesser and R. S. Kody, *Journal of Polymer Science Part B: Polymer Physics*, 1997, **35**, 1611-1619.
65. A. J. Kinloch, S. J. Shaw and D. L. Hunston, *Polymer*, 1983, **24**, 1355-1363.
66. D. W. van Krevelen and K. te Nijenhuis, *Properties of Polymers*, Elsevier, Amsterdam, The Netherlands, Fourth, completely revised edn., 2009.
67. R. F. Fedors, *Polymer Engineering & Science*, 1974, **14**, 147-154.
68. E. Gaudichet-Maurin, F. ThomINETTE and J. Verdu, *Journal of Applied Polymer Science*, 2008, **109**, 3279-3285.
69. A. J. Lesser and K. J. Calzia, *Journal of Polymer Science Part B: Polymer Physics*, 2004, **42**, 2050-2056.
70. S. S. Morye, P. J. Hine, R. A. Duckett, D. J. Carr and I. M. Ward, *Composites Science and Technology*, 2000, **60**, 2631-2642.
71. L. J. Deka, S. D. Bartus and U. K. Vaidya, *Journal of Materials Science*, 2008, **43**, 4399-4410.
72. B. G. Compton, E. A. Gamble and F. W. Zok, *International Journal of Impact Engineering*, 2013, **55**, 11-23.
73. B. R. Lawn, *Journal of the American Ceramic Society*, 1998, **81**, 1977-1994.
74. C. L. Soles, F. T. Chang, B. A. Bolan, H. A. Hristov, D. W. Gidley and A. F. Yee, *Journal of Polymer Science Part B-Polymer Physics*, 1998, **36**, 3035-3048.
75. L. Yang, H. A. Hristov, A. F. Yee, D. W. Gidley, D. Bauchiere, J. L. Halary and L. Monnerie, *Polymer*, 1995, **36**, 3997-4003.
76. B. T. Low, T. S. Chung, H. Chen, Y.-C. Jean and K. P. Pramoda, *Macromolecules*, 2009, **42**, 7042-7054.
77. N. B. McKeown, P. M. Budd, K. J. Msayib, B. S. Ghanem, H. J. Kingston, C. E. Tattershall, S. Makhseed, K. J. Reynolds and D. Fritsch, *Chemistry – A European Journal*, 2005, **11**, 2610-2620.
78. T. W. Sirk, M. Karim, K. S. Khare, J. L. Lenhart, J. W. Andzelm and R. Khare, *Polymer*, 2015, **58**, 199-208.
79. M. Rubinstein and R. H. Colby, *Polymer Physics*, Oxford University Press, New York, 2008.
80. S. Wu, *Journal of Polymer Science Part B: Polymer Physics*, 1987, **25**, 2511-2529.

Changes in $M_{c,a}$ in non-polar ROMP resins correspond to a continuous brittle to ductile transition in contrast to polar thermosets.

